공학박사 학위논문

Preparation and Characterizations of Three Dimensional Nanostructured Carbon Composites as Anode Materials in Li-ion Batteries

리튬 이차전지 음극용 3차원 나노구조의 탄소계 복합물질 제조 및 전기화학적 특성

2013년 2월

서울대학교 대학원

화학생물공학부

박 준 수

Abstract

Preparation and Characterizations of Three Dimensional Nanostructured Carbon Composites as Anode Materials in Li-ion Batteries

Junsu Park

School of Chemical and Biological Engineering

The Graduate School

Seoul National University

The demand for higher specific energy Li-ion batteries for applications such as electric vehicles, next generation electronic devices, and renewable energy sources motivates the research toward electrode materials with larger specific capacities. Among several materials proposed to replace currently available commercial graphite (372 mA h g^{-1}) at the anode electrode, silicon and cobalt oxides have been widely studied as anode materials for use in high performance Li-ion batteries due to their high theoretical capacity of 4200 mA h g^{-1} and 890 mA h g^{-1}, respectively. However, silicon and cobalt oxides have a few problems, including a large volume change during Li insertion/extraction and a poor electrical conductivity. In order to overcome these problems, several studies focused on the possibility of hybridizing silicon and cobalt oxide nanoparticles (NPs) with electrically conducting carbon metrics. Especially, three dimensional (3-D) nanostructure of the ordered mesoporous carbon (OMC) can shorten the Li ion diffusion path and buffer the stress induced by volume expansion, which leads to high specific

capacities.

In this dissertation, the 3-D nanostructured metal or metal oxides/OMC composite prepared by introducing a solvent evaporation induced co-self-assembly strategy are proposed as anode materials and electrode for the Li-ion batteries. This facile, scalable, and one-pot synthesis is using a triblock copolymer as soft template, a resorcinol-formaldehyde polymer as carbon precursor and a metal precursor. And also the preparation of 3-D nanostructured electrode is possible through the combination with a hard template. Details are as follows:

Firstly, the Si NPs trapped in OMC (Si/OMC) composite is prepared by a one-step self-assembly with solvent evaporation. The commercial Si NPs captured by the F127/phenolic resol *via* hydrogen bonding were well-dispersed in the OMC framework through carbonization. The improved electrochemical performances of the composite can be ascribed to the buffering effect of spaces formed in ordered pore channels during the volume expansion of silicon and the rapid movement of lithium ions through the uniform cylindrical pore structure of the mesopores.

Secondly, the Co_3O_4 NPs embedded in the OMC (Co_3O_4/OMC) composite, in which Co_3O_4 NPs with an average size of about below 10 nm are homogeneously embedded in the OMC framework are fabricated. The high capacities of the Co_3O_4/OMC composite can be related to the increased charge storage within the polymer film on the surface of small and well-dispersed Co_3O_4 NPs prepared by a thermal decomposition of a Co^{2+} confined in a polymer framework.

Finally, the 3-D mesoporous carbon nanotube filled with Co_3O_4 NPs (Co_3O_4/MCNT) electrode are prepared by the dual templating method using amphiphilic surfactants (F127) as soft-template and anodic aluminum oxide (AAO) membranes as hard template. The Co_3O_4/MCNT composite exhibit a high reversible capacity because 3-D structured carbon framework allow

direct electronic pathways for efficient charge transport and well-dispersed Co_3O_4 NPs in the MCNT is useful to diminish of surface resistance by formation stable SEI layer.

Keywords: Anode materials, Carbon nanotubes, Li-ion batteries, Ordered mesoporous carbon, Phenolic resol, Three dimensional nanostructure
Student Number: 2009-30243

Contents

List of Tables

List of Figures

Chapter 1. Introduction

1.1 Lithium ion batteries

The Li-ion batteries are efficient, light-weight, and rechargeable power sources for consumer electronics such as laptop computers, digital cameras, and cellular phones [1]. Moreover, they have been intensively studied for use as power supplies of electric vehicles (EVs) and hybrid electric vehicles (HEVs), which require high energy and power densities. Li-ion batteries show the advantages in high cell voltage, high energy and power density. Figure 1-1 shows the schematic of the basic configuration of a Li-ion battery. A Li-ion battery consists of a Li-ion intercalation negative electrode (anode, e.g. graphite) and a Li-ion intercalation positive electrode (cathode, e.g. the lithium metal oxide) having a more positive redox potential. The storage capacity of a battery is given by the amount of Li that can be stored reversibly in the two electrodes. These electrodes are separated by an electrolyte typically contains lithium salts dissolved in an organic carbonate solution (e.g. $LiPF_6$ in ethylene carbonate-diethylcarbonate). It should be a good ionic conductor and electronic insulator. Li-ion batteries operate by reversibly intercalating Li ions in each of the two electrodes. Intercalation is a process by which guest species (Li ions) reversible insert/extract from the host matrix (electrode material) without significantly changing the structure of the host. Upon charging, Li-ions are released by the cathode and

intercalated at the anode. When the cell is discharged, Li-ions are extracted by the cathode and inserted into the anode.

Electrode materials must fulfill three fundamental requirements to reach the goal of a high specific energy and energy density: (1) a high specific charge and charge density, that is, a high number of available charge carriers per mass and volume unit of the material; (2) a high cell voltage, resulting from a high (cathode) and low (anode) standard redox potential of the respective electrode redox reaction; and (3) a high reversibility of electrochemical reactions at both cathodes and anodes to maintain the specific charge for hundreds of charge–discharge cycles [2].

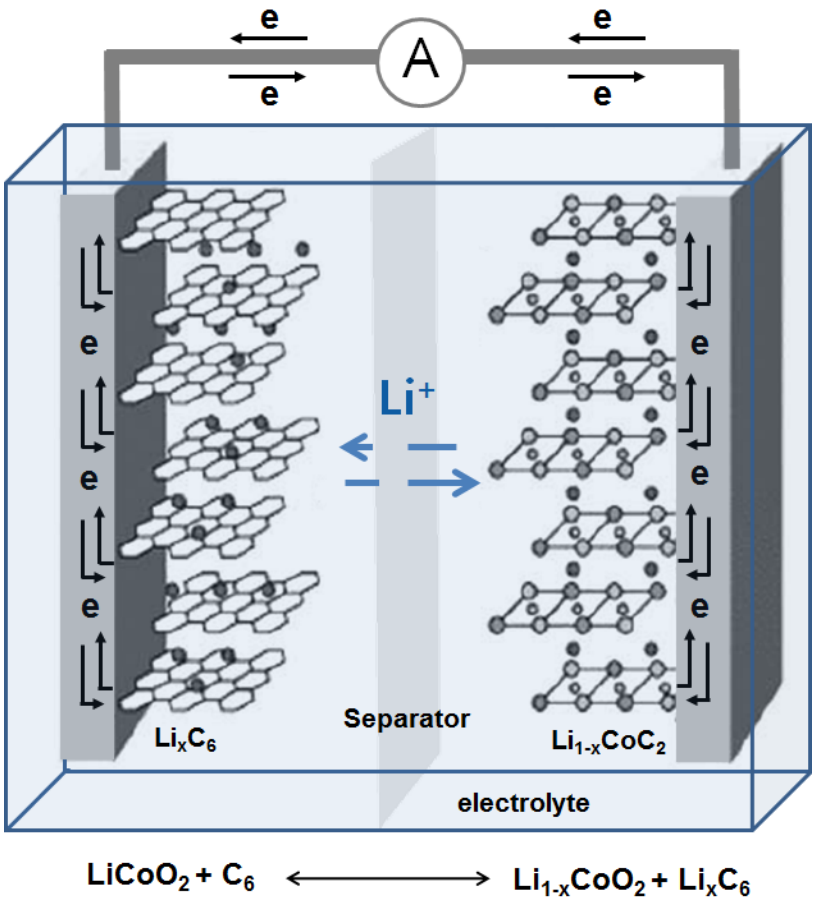

Figure 1-1 Schematic diagram of the chemical reaction of the Li-ion batteries.

1.2 Three-dimensional (3-D) nanostructured electrode

Li-ion batteries are operated by insertion processes of Li ions in an electrolyte between anode and cathode electrode, which arranged in a 2-D parallel-plate configuration in the cells. The composite electrodes of conventional 2-D thin film batteries contain an active material, an electronic conductor, and a binder phase. Li-ion can diffuse through the remnant porosity of the composite electrode. The composite electrodes need larger footprint areas which can involve a higher amount of the active material to deliver high capacities. Therefore, thicker electrodes can provide high energy density but also induce the internal power losses by a slow diffusion of Li ions or electrons inside the thick electrode [3]. However, the reducing thickness of the electrode may induce lower energy capacity and shorter operating time due to the limitation in footprint area. Improved battery performance might be realized through alternative designs of electrodes. The 3-D nanostructured electrode can effectively increase energy density and high-rate discharge capabilities because the 3-D architectures can not only increase the amount of active material within a given footprint area but also shorten the diffusion length path of Li ions [4]. When 1-D and 3-D nanostructure are combined, the additional thickness of electrode can increase the amount of electrode material within a given footprint area and thus increase the areal capacity.

1.3 Template synthesis of carbon nanocomposite

1.3.1 Soft template synthesis

Ordered mesoporous materials have received enormous attention due to their high surface areas, regular frameworks, and large pore sizes with narrow distribution [5]. Ordered mesoporous carbon, which is one of the most promising materials, possesses both remarkable functional properties and excellent chemical/thermal stability, which makes it suitable for applications in catalysis, [6] bioreactor construction, [7] and energy storage [8]. However, the preparation of mesoporous carbon materials with ordered open pore structures is extremely difficult in solution and remains challenging because of the high formation energy of C-C bonds. A frequently used approach to fabricate ordered mesoporous carbon materials is a nanocasting procedure with utilizes mesoporous silicate as a hard template [9]. It is an elaborate, high-cost, and industrially unfeasible method. Therefore, a soft supramolecular self-assembly approach toward ordered mesoporous carbons is desirable.

Evaporation-induced self-assembly (EISA) process enables the fast production of patterned porous or nanocomposite materials in the form of films, fibers, or powders [10]. A general definition of self-assembly is the spontaneous organization of materials through noncovalent interactions (hydrogen bonding, Van der Waals forces, electrostatic forces etc.) with no external intervention. Oraganic-orgainc self-assembly has been applied to synthesizing organic nanostructures and carbon materials via carbonization.

Self-assembly typically employs asymmetric molecules that are pre-programmed to organize into well-defined supramolecular assemblies. Most common are amphiphilic surfactant molecules or polymers composed of hydrophobic and hydrophilic parts [11]. The PS-P4VP/resorcinol-formaldehyde system was the first report on the synthesis of highly ordered mesoporous carbon materials through soft templates [12]. Hydrogen bonding was utilized to preferentially organize the resorcinol polymer precursor into the P4VP domain. Resorcinol was then polymerized with formaldehyde to form a carbon precursor with a high carbon yield. Tanaka et al. were the first to report the successful synthesis of ordered porous carbon films using a Pluronic surfactant template (F127) [13]. Zhao's group reported soft template synthesis of highly ordered mesoporous carbon materials with PEO-PPO-PEO triblock copolymers as templates (PPO: polypropyleneoxide; PEO: polyethyleneoxide) [14]. PPO-PEO-PPO triblock copolymers are another family of commercial surfactants that have the hydrophilic PEO block located in the middle and the hydrophobic PPO blocks at either end of the polymer chain. Self-assembly is begun with a homogeneous solution of PPO-PEO-PPO triblock copolymer (F127) and phenolic resol precursors in ethanol solvent. During evaporation of ethanol, the concentration of triblock copolymer progressively exceeds the critical micelle concentration, resulting in micelle formation (Figure 1-2(a)). Phenolic resol precursors can interact with the reverse triblock copolymer template by forming hydrogen bonds between the hydroxyl groups of the resol units and the PEO segments of the template. Upon continued solvent

evaporation an organic–organic composite liquid-crystal mesophase with a high curvature is formed (Figure 1-2(b)) [15]. The phenolic resol precursors around the templates are thermo-polymerized by heating at 100–160 °C and the mesostructured frameworks become rigid. At temperature of 350 °C, the template is removed. The mesoporous carbon frameworks were obtained in a subsequent carbonization step at 600–1000 °C with a very slow heating rate under nitrogen (Figure 1-2(c)).

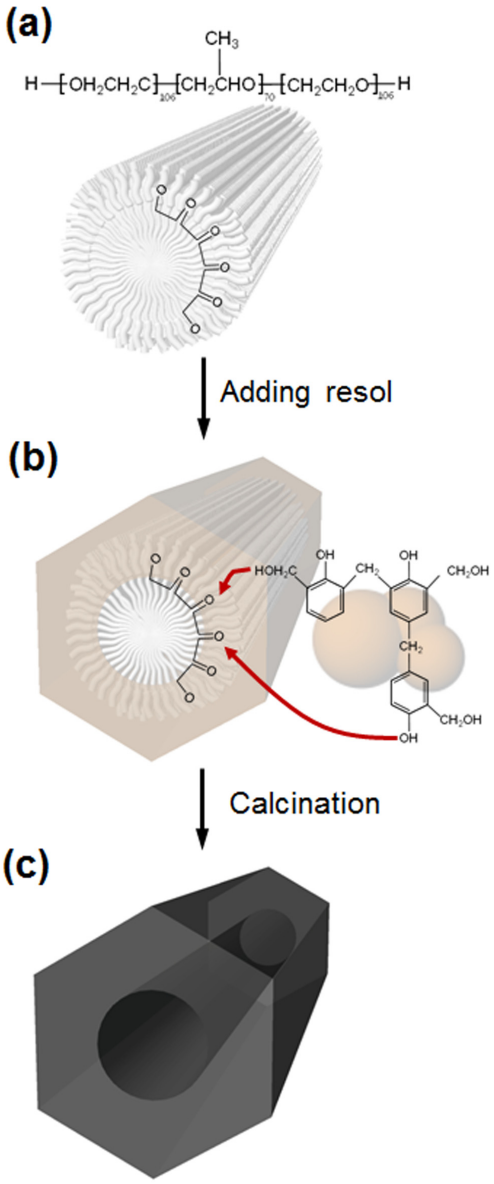

Figure 1-2 Scheme for the preparation of the ordered mesoporous polymer resins and carbon frameworks by soft template synthesis using triblock copolymer (F127) and phenolic resol.

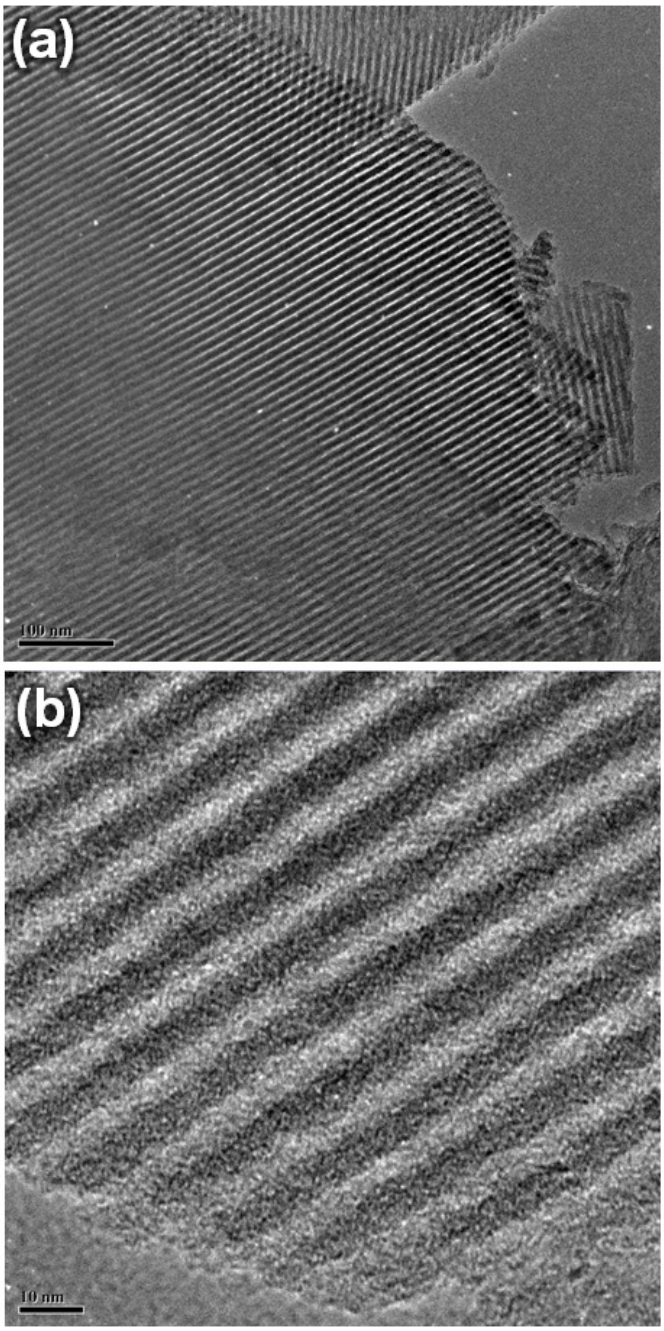

Figure 1-3 HR-TEM images of ordered mesoporous carbon prepared by soft template method.

1.3.2 Hard template synthesis

The use of templates is one of the main strategies for the fabrication of advanced materials with new nanostructures that have attracted considerable research effort. Templates can be classified as 'hard' and 'soft'. Hard templates are usually solid-state materials with particular structure and morphology, whereas soft templates are generally in a fluid-like state [16]. Micro- and nanoporous templates are routinely used to fabricate one-dimensional materials because their pores can be filled with a variety of materials using a number of techniques [17]. Hard templating is usually consists of the following steps (Figure 1-4): a. Preparation of hard templates; b. Coating the templates with the target material; and c. Selective removal of the templates [16]. The anodic aluminum oxide (AAO) membrane is one of the widely used nanopore templates. It is fabricated by anodization of aluminum metal in an acidic environment which causes the metal to be etched into a porous structure. The aluminum anodization is highly systematic, which generates a highly-ordered hexagonal pore array with cylindrical pore shapes. They can easily be fabricated by a controlled anodization process and have been well characterized in the last decades. These alumina template are commercial available as filter membranes (Whatman) as shown in Figure 1-5(a). The general procedure for hard template synthesis involves the use of a porous membrane with cylindrical, monodisperse macropores. The electrode active material is filled into each pore by using chemical or electrochemical deposition method. And then, the template is removed by plasma etching or chemical dissolution. After removal of the template, the resulted material maintains the fibrous or tubular structure (Figure 1-5(b-d)).

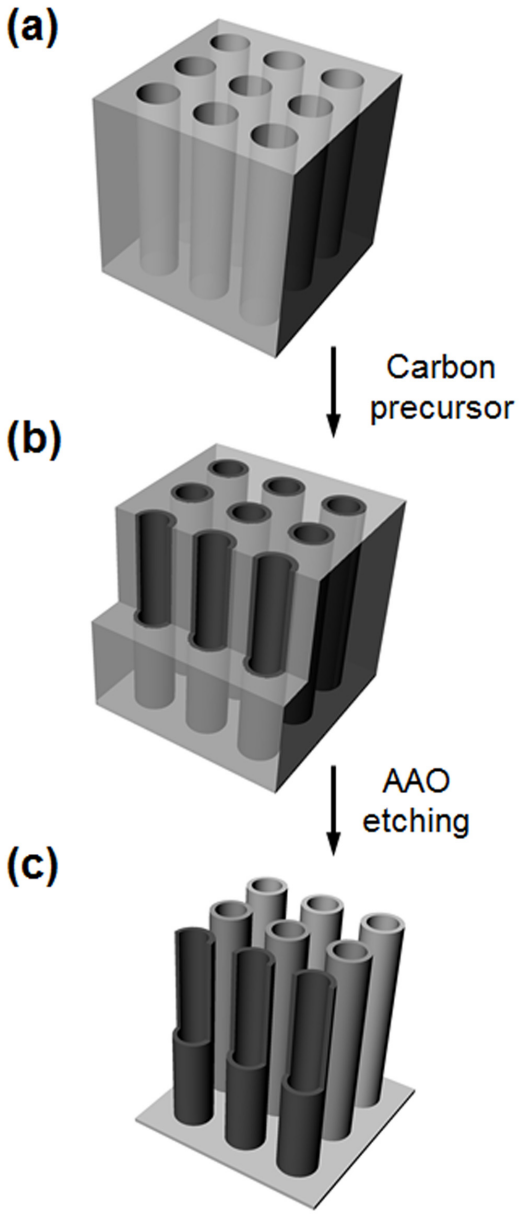

Figure 1-4 Scheme for the preparation of the carbon nanotube array by hard template synthesis using the AAO.

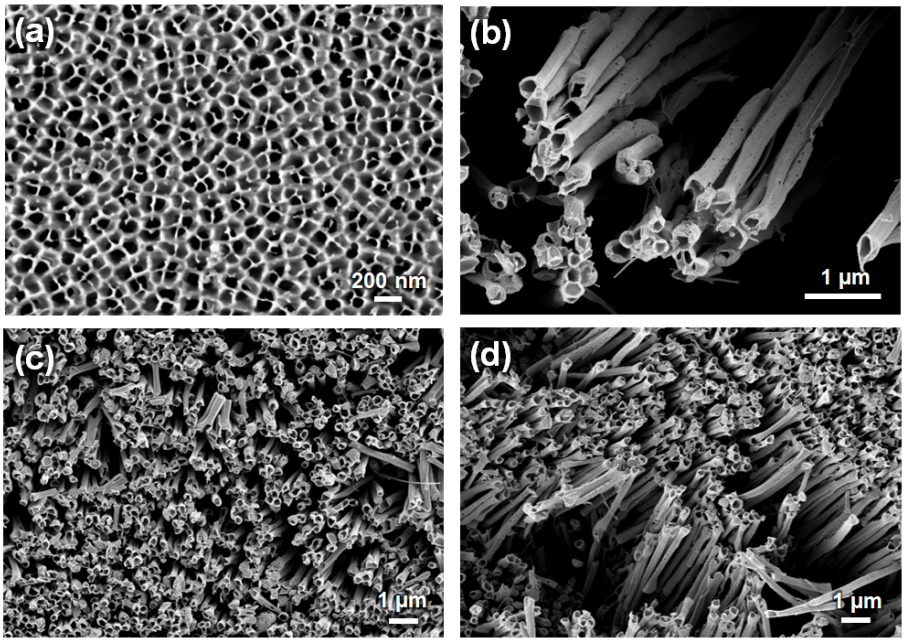

Figure 1-5 SEM images of (a) a commercial AAO membrane with pore size of 200 nm and (b-d) carbon nanotube array prepared by hard template method.

1.4 Objectives

The thesis mainly consists of developing 3-D nanostructured carbon composite as anode materials in high performance Li-ion batteries. The objectives of this thesis are summarized as follows;

1) to fabricate Si nanoparticles trapped in ordered mesoporous carbon composite.
2) to fabricate Co_3O_4 nanoparticles embedded in mesoporous carbon composite. Small and well-dispersed Co_3O_4 nanoparticles prepared in carbon pore wall
3) to fabricate 3-D aligned mesoporous carbon nanotube filled with Co_3O_4 nanoparticles by AAO template assisted co-self-assembly process.

Chapter 2. One-pot synthesis of Si nanoparticles Trapped in Ordered Mesoporous Carbon and Its Use as an Anode Material in Li-ion Batteries

2.1 Introduction

The development of high-performance Li-ion batteries is urgently needed for various applications, such as portable electronics and electric vehicles [18,19]. However, the low capacity (372 mA h g^{-1}) of the currently used graphite anodes is clearly a limiting factor in the development of high-performance Li-ion batteries. One of the most promising candidates for an anode material that could replace graphite is silicon (Si), an element that has a high theoretical capacity (ca.4200 mA h g^{-1}) [20]. However, during the Li alloying and dealloying steps, Si undergoes a significant volume expansion (>300%), which leads to pulverization and loss of electrical contact, resulting in capacity fading [21]. Many methods have been proposed for effectively reducing this volume expansion, in attempts to utilize Si as an anode material. Among these strategies, carbon-Si composites such as Si@C core-shell nanowires [22], Si/graphene composites [23], Si/graphite composites [24], carbon nanotubes coated with Si [25], and Si/C composite nanofibers [26], prepared using various carbon precursors have been extensively investigated. There are several reasons for using carbon; first, it can accommodate the volume expansion of Si; second, it has a high

electrical conductivity; lastly, it minimizes capacity loss with the formation of stable solid electrolyte interphase (SEI) layers in aprotic organic electrolytes [27]. These methods have shown an improved electrochemical stability of Si as a proof-of-concept. However, these techniques are not suitable for large scale production due to the production of pollutants (e.g. strong acid) associated with their production, and multiple production processes. Therefore, particulate hierarchical nanostructure composites such as mesoporous composite are currently of interest as attractive candidates for large-scale applications [27]. Metal or metal oxide/ordered mesoporous carbon (OMC) composites based on CMK-3 have recently been reported as anode materials, due to their uniform pore channels, very high pore volume and interconnected porous structure [28-31]. CMK-3, an ordered mesoporous carbon, is prepared by applying mesoporous silica as a template and sucrose as the carbon source via an impregnation procedure [32]. In this study, we report, for the first time, on the design and preparation of Si nanoparticles (Si NPs) trapped in OMC (Si/OMC composite). Si nanoparticles captured by the F127/phenolic resol by hydrogen bonding were well-dispersed in the ordered mesoporous carbon framework through carbonization. The products display a high capacity and stable cyclic performance. They therefore have potential for use as an advanced anode material for lithium ion batteries. The major advantages of the Si/OMC composite are ease of synthesis using commercial Si NPs, and the potential for large scale production, as verified by a recent report on the preparation of OMC on a kilogram scale [33].

2.2. Experimental

2.2.1. Preparation of Si/OMC composite

Si/OMC composite was prepared by the co-assembly of a phenol resol, Pluronic F127 and Si nanoparticles, followed by carbonization. The phenolic resol precursor was prepared by polymerizing phenol (0.46 g, 4.88 mmol) and formaldehyde (37 wt%, 0.79 g) containing formalin (9.75 mmol) by a base-catalyzed method as described previously [34]. The mesostructured polymer-resols were templated using a triblock copolymer F127. F127 (0.63 g) was dissolved in 12.6 g of ethanol. Ethanol solution of the resol precursors was added under stirring for 30 min to form a homogeneous solution (phenol/formaldehyde/NaOH/F127 = 1:2:0.1:0.012 in mole ratio). The native oxide layer on the surface of Si NPs (Alfa aesar) is helpful, in that it interacts strongly with the resol, which has a large number of hydroxyl groups (-OH) by the formation of hydrogen bonds, thus permitting it to dissolve completely in ethanol [35]. Si NPs were dispersed in ethanol by sonicating the solution for one hour. A 0.3 g of Si NPs was added to a stirred ethanol solution of resol and F127. The mixture was transferred to a dish and the ethanol allowed evaporating at ambient temperature for 8 h. The resulting membrane was heated in an oven at 120℃ for 24 h for thermopolymerization. The products were calcined at 350℃ for 5 h at a heating rate of 1℃ min^{-1} to remove the triblock copolymer template under a stream of argon. The preparation was finally heated from 350 to 900℃ at a rate of 1℃ min^{-1} and the final temperature was held for 4 h to allow the preparation to carbonize. Based on a

thermogravimetric analysis (TGA), the weight percentage of OMC and Si in the Si/OMC composite was estimated to be 50.5 and 49.5%, respectively (Figure 2-1). In order to identify the effect of OMC, the Si/OMC composites were prepared with different Si contents: 40, 65, and 82 wt%, respectively. The Si contents were calculated based on the amount of carbon precursor and Si NPs and precisely controlled during the synthesis. After preparation of the Si/OMC composites, the loading Si amount of the samples was determined by the TGA analysis. (Figure 2-2). The non-porous carbon/Si composite was prepared to compare the electrochemical properties with the Si/OMC composite. It was synthesized following the same procedure, but without the presence of F127 (Figure 2-3).

2.2.2. Characterization of Si/OMC composite

The Si/OMC composite was characterized by field-emission scanning electron microscopy (SEM, Carl Zeiss, SUPRA-55VP) and high-resolution transmission electron microscopy (HR-TEM, Jeol, JEM-3010). Small angle and wide angle X-ray diffraction (XRD) patterns were obtained by a small-angle X-ray scattering (SAXS) with General Area Detector Diffraction System (Bruker, GADDS) and M18XHF-SRA diffractometer (MAC Science), respectively. N_2 adsorption–desorption isotherms were measured with a Micromeritics ASAP 2010 instrument. The Brunauer-Emmett-Teller (BET) method was utilized to calculate the specific surface area. The pore volume and pore size distributions were derived from the adsorption branches of the isotherms using the Barrett-Joyner-Halanda (BJH) method. TGA was

performed using a thermogravimetric analyzer (Versa Therm, Thermo Scientific) with a heating rate of 5℃ min^{-1}. Electrochemical characterizations were performed using coin-type half cells (2032 type) prepared in argon-filled glove box that contained an electrode, lithium foil (Alfa aesar) as counter electrode, a microporous polyethylene separator, and an electrolyte solution of 1 M $LiPF_6$ with 1:1 w/w ethylene carbonate:diethyl carbonate (Panax e-tec). The electrode was composed of Si/OMC composite (70 wt%), poly (vinylidene fluoride) binder (20 wt%), and Super P carbon black (10 wt%), respectively. The cells were discharged (Li-ion insertion) and charged (Li-ion extraction) in a voltage range from 0.01 to 2.0 V (vs. Li/Li+) using a battery tester (WBCS3000, Wonatech). The capacity values were calculated based on the mass of the active materials.

2.3. Results and discussion

The Si/OMC composite was prepared by a one-pot synthesis by means of a solvent evaporation induced self-assembly method using a phenolic resol as the carbon source, a triblock copolymer Pluronic F127 as a structure-directing agent and Si NPs with sizes of approximately 50 nm [36] (Figure 2-4). F127 was dissolved in ethanol (Figure 2-4(a)). The phenolic resol and Si NPs were added and the mixture was stirred. The solution was then aged at room temperature to evaporate the ethanol. During the evaporation of ethanol, the resol-copolymer composite is transformed into an ordered liquid crystalline mesophase. The Si NPs are coated with the liquid crystalline mesophase because the liquid crystalline mesophase contains a large number of hydroxyl groups (-OH) that can interact with native oxide layer on the surface of Si NPs by hydrogen bonding [35]. (Figure 2-4(b)). During the aging at 120℃ for thermopolymerization, the integral 3-D resin frameworks are finally formed [3517]. (Figure 2-4(c)). After calcination, the Si NPs are distributed in the OMC frameworks formed by decomposition of the template F127 and carbonization of the crystalline mesophase (Figure 2-4(d)). This mechanism makes it possible to trap nanoparticles that have a larger diameter than the pore size in the OMC structure, which is difficult in the case of CMK-3. HR-TEM images of the Si/OMC composite support the conclusion that Si NPs are trapped in the OMC framework after calcination at 900°C. Figure 2-5(a-c) show that the ordered hexagonal mesoporous carbon and Si NPs, which are observed as dark spots, are dispersed in the OMC. The presence of partially

mesostructural irregularities around the Si NPs suggests that the Si NPs are located within the OMC framework. The lattice fringes of the (111) plane, corresponding to the d spacing of 3.0Å, are observed for the Si NPs across the OMC walls (Figure 2-5(c)). Metal or metal oxide/CMK-3 composites can be synthesized only if the sizes of the metal or metal oxide particles are smaller than the pore size (ca. 5 nm) of the CMK-3, due to the mechanical stability of the pore wall [37]. Therefore, preparing metal or metal oxide/CMK-3 composites using commercial nanoparticles with diameters greater than 5 nm is difficult. Si NPs in the Si/OMC composite do not exist inside the pore of OMC, unlike metal or metal oxide/CMK-3 composites. The Si NPs are surrounded by an OMC framework because the Si NPs were coated with the liquid crystalline mesophase as the result of the evaporation induced self-assembly. It can be clearly identified by HR-TEM image of Si/OMC composite with 82 wt% Si contents (Figure 2-6(a)). The presence of partially mesostructural irregularity around the Si NPs suggests that they are located in the OMC framework, in the case of the Si/OMC composite with a 50 wt% Si content (Figure 2-6(b)).

Figure 2-7(a) show small-angle XRD patterns of OMC and Si/OMC composite. OMC exhibits peaks indexed as (10), (11) and (20) associated with well-ordered hexagonal (p6m) mesostructure [37]. However, the Si/OMC composite displays only a small (10) peak due to the increase in the mesostructural irregularity with the presence of Si NPs. A wide-angle XRD pattern of the Si/OMC composite exhibited sharp peaks corresponding to crystalline Si at around 28°, 47°, 56°, 69°, and 76° which correspond to the

(111), (220), (311), (400), and (330) plane [38], as shown in Figure 2-7(b). Two diffraction peaks at around 21° and 43° are assigned to the (002) and (100) plane for carbon materials [39]. The XRD patterns of the Si/OMC composite confirm the presence coexistence of two phases, namely, crystalline Si and carbon. Figure 2-7(c) provides information on nitrogen sorption isotherms and the pore size distribution of the OMC and Si/OMC composite. While the OMC exhibits a type IV isotherm with H2 hysteresis loops, indicating the presence of relatively uniform mesopores, the Si/OMC composite shows a H3 hysteresis loop which does not exhibit any limiting adsorption at high p/p_0, due to the filling of interparticle textural pores [40]. The pore size distribution and average pore size of the Si/OMC composite are wider and larger than those for OMC, respectively (Figure 2-7(d)). This indicates the degradation of mesostructural regularity by Si NPs located in the OMC. The Si/OMC composite has a BET surface area of 371.9 $m^2 g^{-1}$ and a pore volume of 0.39 $cm^3 g^{-1}$, values that are lower than those of the OMC (602.0 $m^2 g^{-1}$ and 0.45 $cm^3 g^{-1}$). The decrease in BET surface area and pore volume demonstrate that the pores of the OMC are partially filled with Si NPs [28].

Figure 2-8(a-c) show galvanostatic discharge/charge curves for commercial Si NPs , OMC, and Si/OMC composite from 0.01 to 2.0 V (vs. Li/Li+) after 1, 2, and 50 cycles. For the 1st discharge, the Si NPs in the OMC framework form a two-phase structure of partially lithiated Si and unlithiated crystalline Si produced by the diffusion of Li ions [41]. Therefore, Si NPs and Si/OMC composite display a long voltage plateau at 0.1 V, consistent with the typical

characteristics of crystalline Si [41]. However, an obvious voltage plateau was not observed for OMC (Figure 2-8(b)). The Si/OMC composite (Figure 2-8(c)) exhibits an initial discharge capacity of 1275 mA h g^{-1} at 0.1C. The 1st discharge capacity of the Si/OMC composite is lower than that of Si NPs (Figure 2-8(a)). The irreversible capacity in the first cycle induced by SEI formation on the large surface of Si/OMC composite is similar level to other Si/carbon composites [42,43]. However, during further cycling at 1C, the Si/OMC composite exhibits more stable cycling properties than Si NPs after 50 cycles. Fig. 3d displays differential capacity plots of Si/OMC composite during 1, 2, 5, and 20 cycles. During the 1st discharge, the crystalline Si NPs in the OMC form an alloy with Li ions and the crystalline Si then undergoes solid state amorphization, due to the large atomic displacement of Si atoms [44]. This reaction occurs at a peak potential of ~0.018 V with an onset potential of 0.10 V. In addition, Li_xC_6 is formed by the intercalation reaction of Li ions with the OMC, which occurs at a peak potential of 0.78 V (Figure 2-9). The first cathodic peak of the Si/OMC composite is shifted from 0.09 V to 0.018V and an additional new peak appears at 0.78 V, in comparison with that of the Si NPs (Figure 2-10) due to differences in surface kinetics between the Si/electrolyte and Si/OMC/electrolyte [45]. Upon the 2nd discharge, two peaks at 0.08 and 0.22 V, corresponding to the nucleation and growth of other intermetallics/amorphous Li_xSi phase, are observed [44]. In addition, the difference curve for the charge shows two peaks at 0.3 and 0.48 V, corresponding to de-lithiation of the alloy to amorphous Si [46]. These peaks from the 5th to 20th cycle do not change significantly, unlike those of Si NPs.

The buffer effect of the OMC on the volume expansion of Si was examined through a comparison of its electrochemical stability as a function various wt% Si contents (Figure 2-8(e)). Rate 0.1C calculated by the ratio between Si and carbon of each sample was used for the first cycle and the first charge capacity was increased with an increase in the wt% Si content. After the first cycle, the charge/discharge rate was increased to 1C. After the 10th charge, the capacity was decreased dramatically due to the volume expansion of Si. The Si/OMC composite with below 50 wt% Si content exhibited a stable capacity after 30th cycles. These results prove that the carbon content of Si/OMC composite accommodates the stress with volume expansion and that this improves the electrochemical stability of the composite. The Si/OMC composite with 50 wt% Si content displayed the highest capacity and stability. Figure 2-11(a) shows the cycling performance of Si/OMC composite with 50 wt% Si content and the Si NPs coated with non-porous carbon (Si@C) composite. The reversible capacity of the Si/OMC composite increased with cycling and maintained above 700 mA h g^{-1} for 50 cycles. The coulombic efficiency after first cycle at 0.1C rate becomes stable in the range of 94-100% at 1C rate. The cycling performance of the Si@C composite synthesized without the presence of F127 was tested to identify the effect of mesopore structure on the capacity. The initial discharge capacity of Si@C composite was approximately 260 mA h g^{-1}, followed by a low capacity (~130 mA h g^{-1}) for 50 cycles. A thick non-porous carbon layer of Si@C composite can act as a barrier for Li ion diffusion [47]. Therefore, the higher capacity of the Si/OMC composite can be attributed to the ordered mesopore structures

that facilitate the uniform penetration of electrolytes into the mesopores and the thin pore walls, which ensure short diffusion paths for Li ions, resulting in a high transfer rate of Li ions into Si NPs [28]. Figure 2-11(b) exhibits the rate capability of the Si/OMC composite operated at various rates between 1.5 and 3C. The reversible capacity of the Si/OMC composite is 496 mAh g^{-1} for the 10th cycle at 1.5C, 524 mAh g^{-1} for the 20th cycle at 2C, 504 mAh g^{-1} for the 30th cycle at 2.5C, and 499 mAh g^{-1} for the 40th cycle at 3C. Moreover, when the rate returns to the initial 1.5C after 40 cycles, the composite electrode recovers its original capacity (590 mAh g^{-1} for the 50th cycle). In order to further investigate the effect of OMC structure on stress absorption with volume expansion, the morphology of a Si/OMC composite after cycling test was examined by obtaining SEM and HR-TEM image (Figure 2-12). The SEM image shows the SEI layer formed on the surface of the Si/OMC composite (Figure 2-12(a)). After cycling test, the pore structures are clearly observed and Si NPs located in the OMC framework are visible (Figure 2-12(b)). However, empty spaces (light areas) generated by the expansion of Si NPs during the initial cycle, and surroundings of the Si NPs inside the Si/OMC composite are also observed. Importantly, these empty spaces could act as a buffer space for the Si expansion during electrochemical cycling without breaking of the OMC framework. In addition, it provides the formation of a stable SEI on the surface of the OMC and prevents the continual rupturing and reformation of the SEI [42, 48].

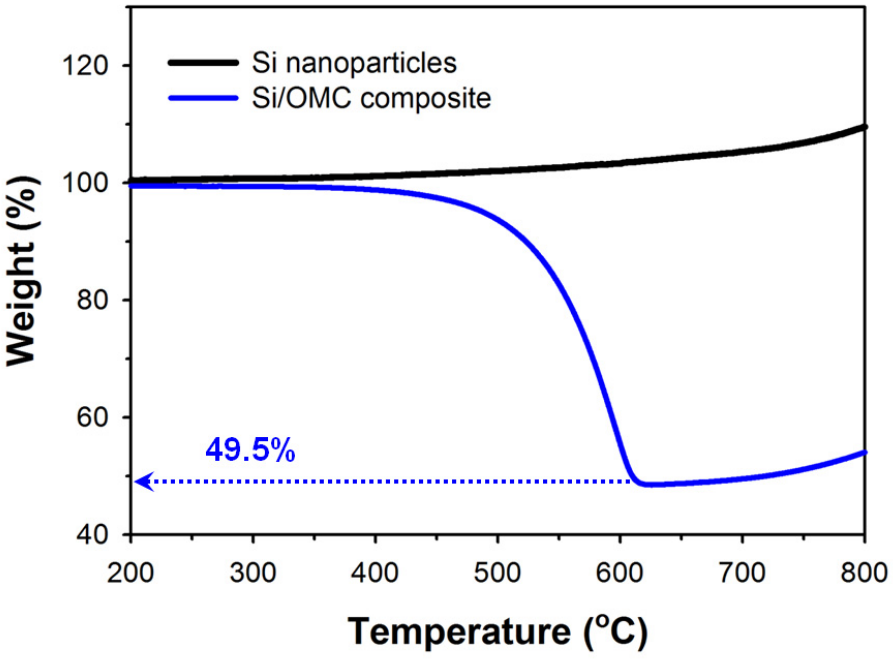

Figure 2-1 TGA analysis of Si NPs and Si/OMC composite.

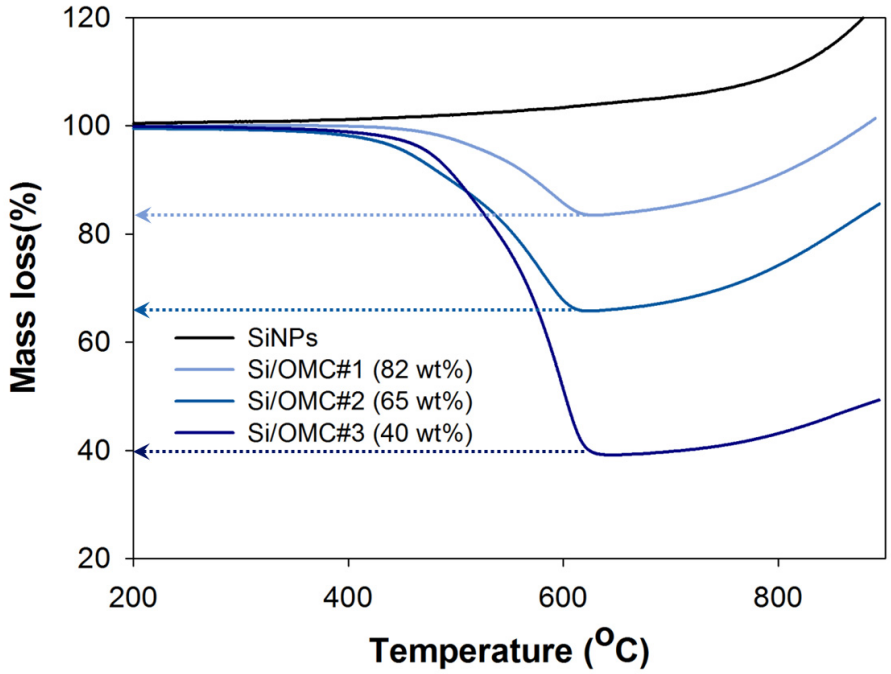

Figure 2-2 TGA analysis of Si NPs and Si/OMC composites with different Si contents.

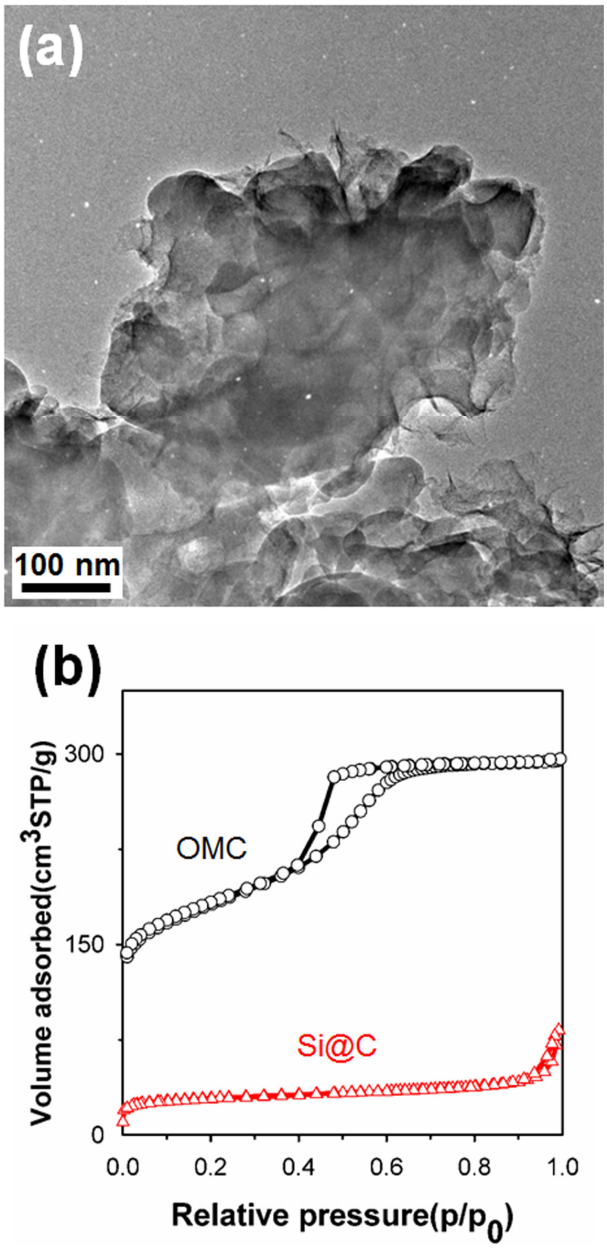

Figure 2-3 (a) HR-TEM images of the Si NPs coated with non-porous C (Si@C) composites. (b) N_2 adsorption/desorption isotherms of OMC and the Si@C composites.

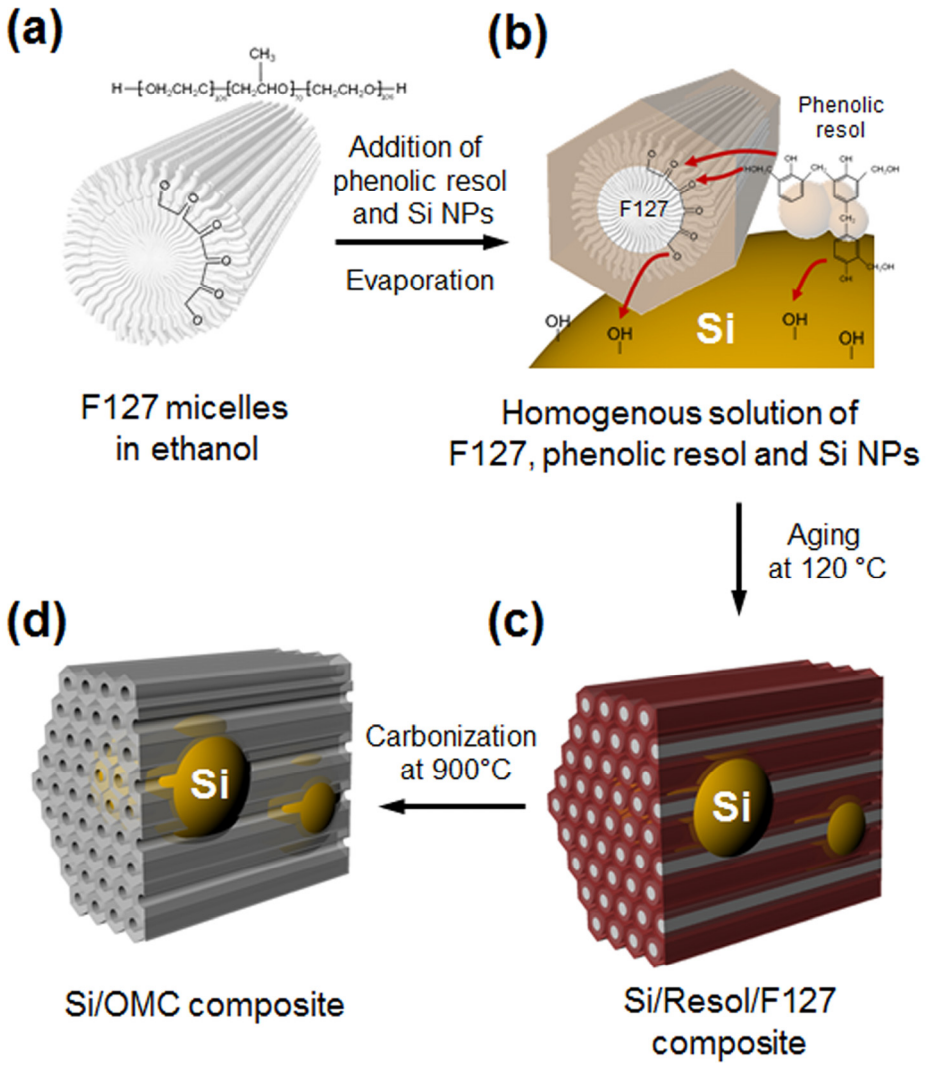

Figure 2-4 Schematic diagram for the synthesis of the Si/OMC composite.

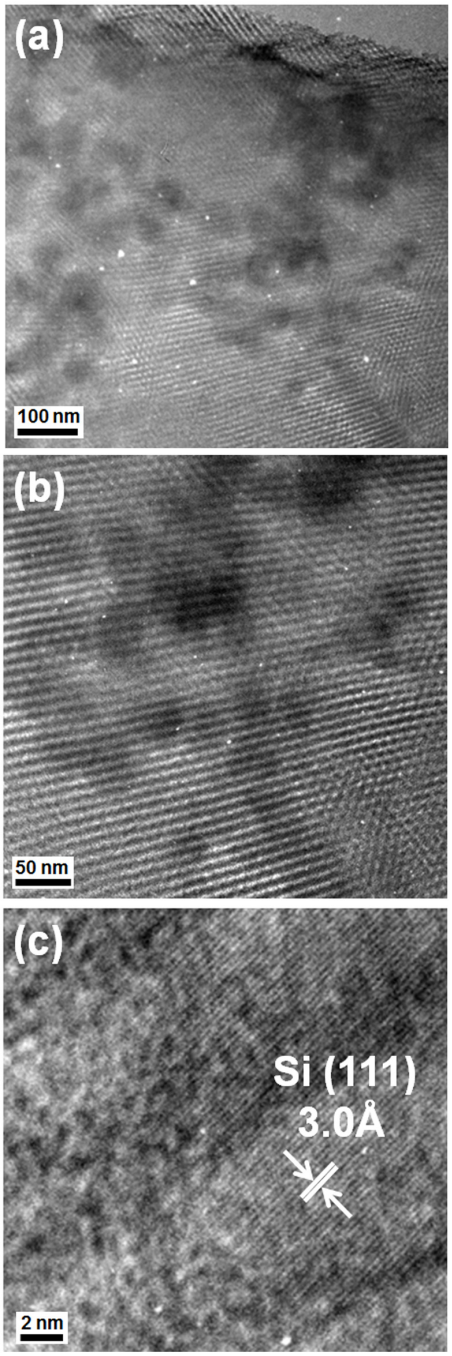

Figure 2-5 (a-c) HR-TEM images of the Si/OMC composite.

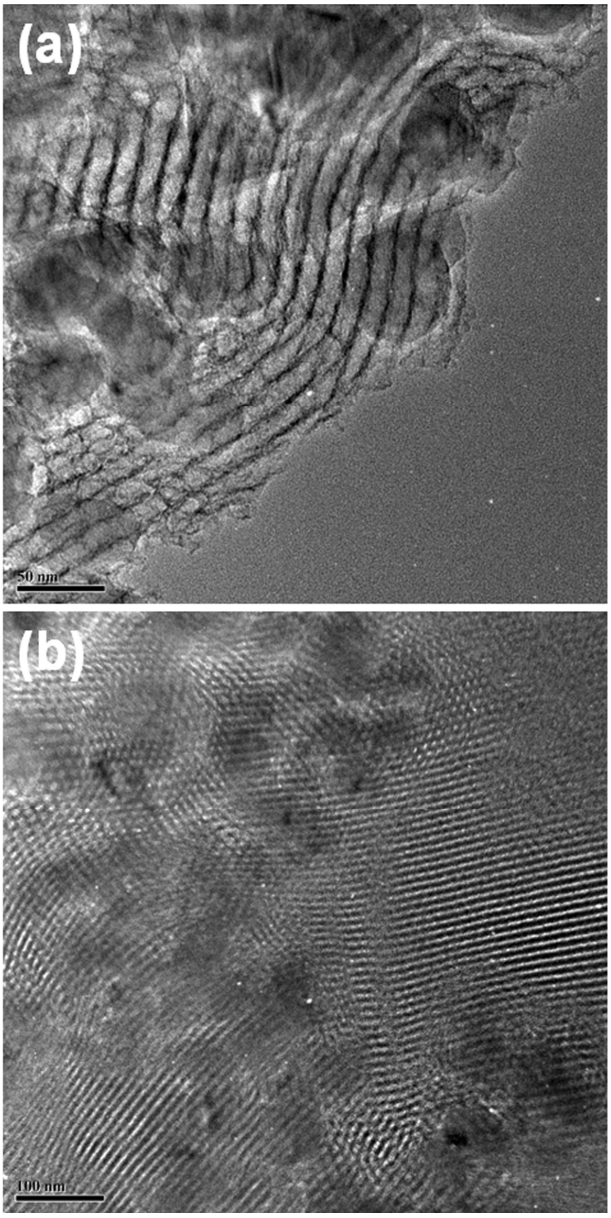

Figure 2-6 (a) HR-TEM images of the Si/OMC composites with (a) 80 wt% and (b) 50 wt% Si contents, respectively.

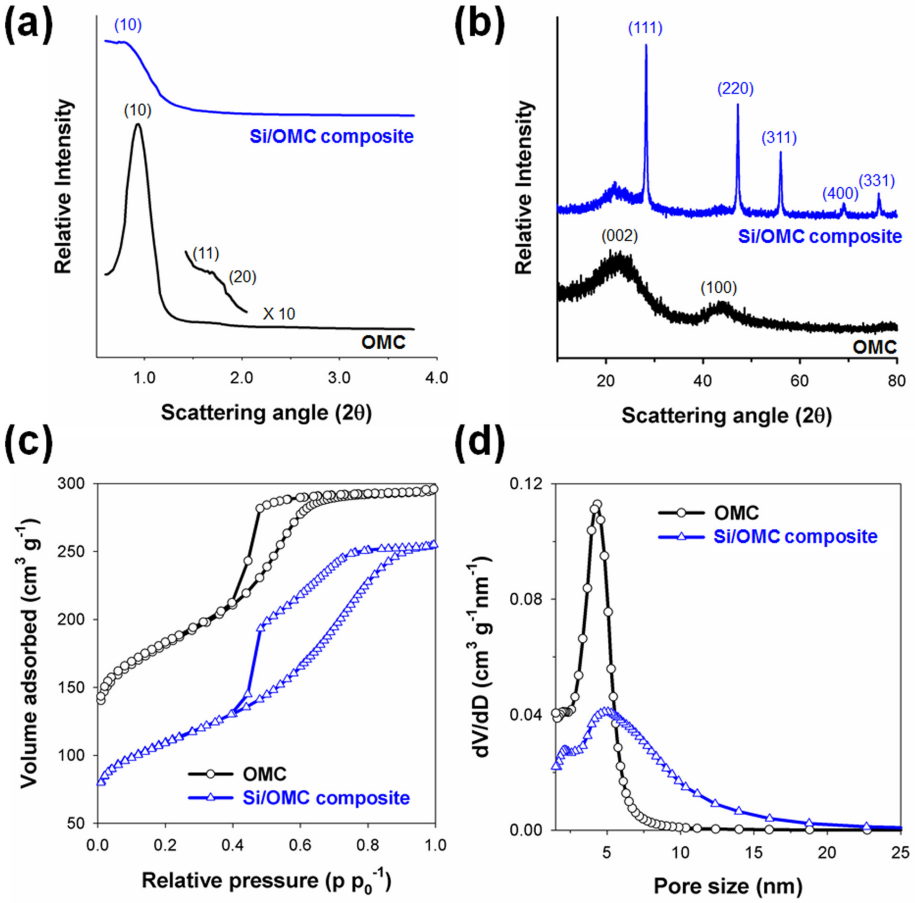

Figure 2-7 (a) Small-angle and (b) wide-angle XRD patterns of OMC and Si/OMC composite. (c) N_2 adsorption/desorption isotherms and (d) pore size distribution of OMC and Si/OMC composite.

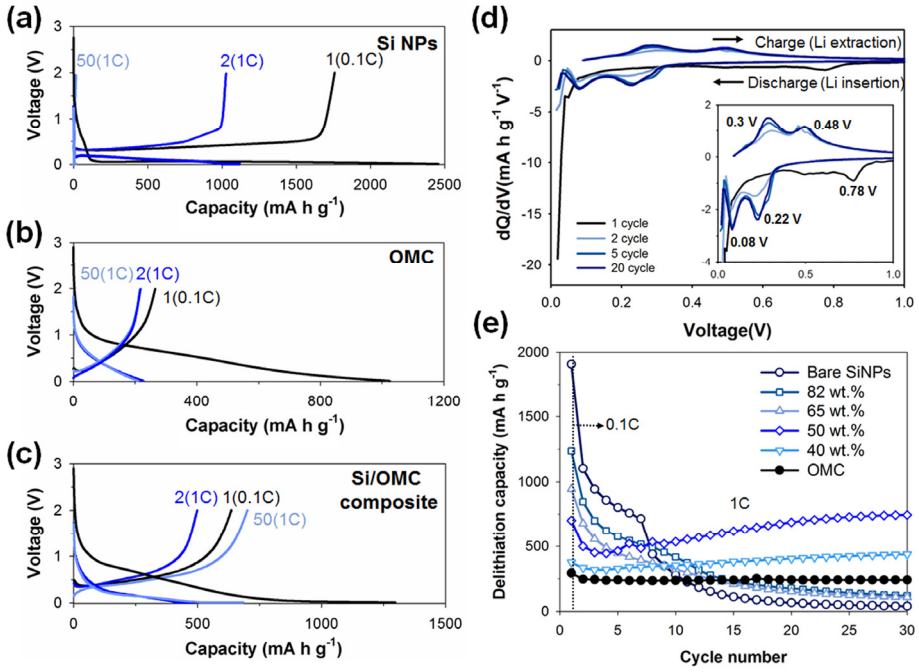

Figure 2-8 Voltage profiles of (a) commercial Si NPs, (b) OMC, and (c) Si/OMC composite during the 1st, 2nd, and 50th cycles. (d) Differential capacity plot of Si/OMC composite during the 1st, 2nd, 5th, and 20th cycles. (e) Galvanostatic cycling of Si/OMC composite with different Si contents.

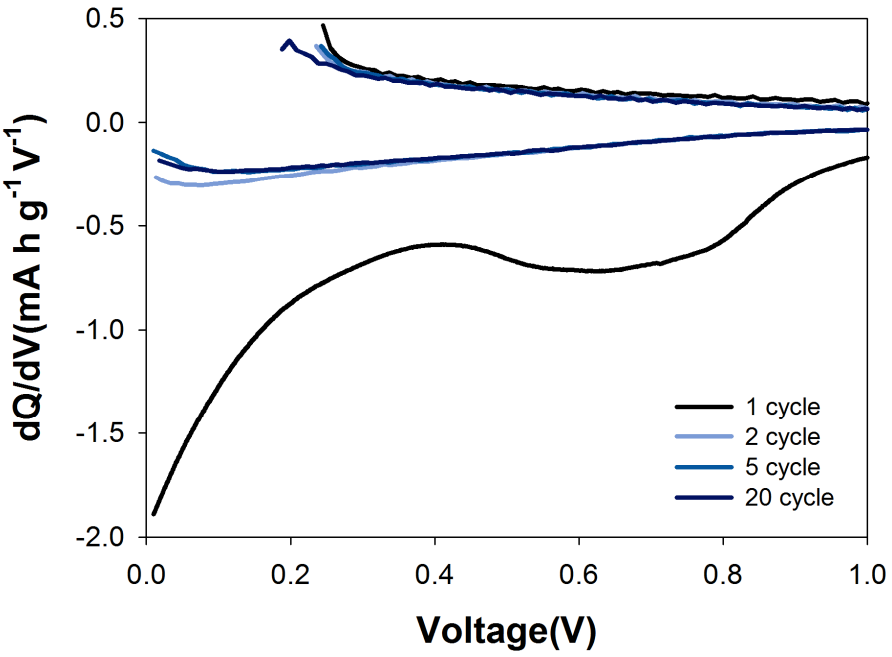

Figure 2-9 Differential capacity plot of OMC during the 1st, 2nd, 5th, and 20th cycles.

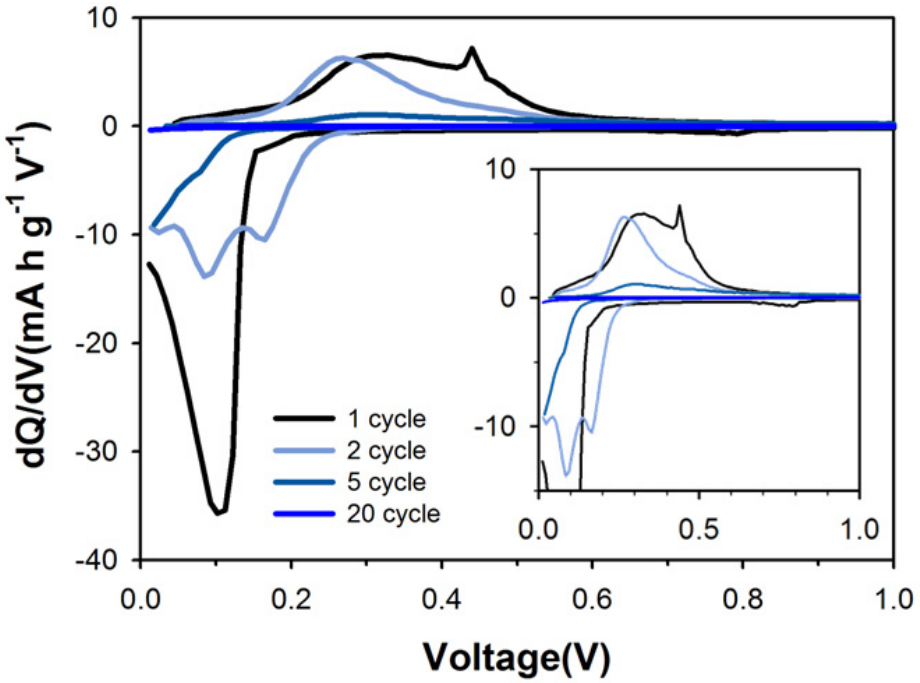

Figure 2-10 Differential capacity plot of Si nanoparticles during the 1st, 2nd, 5th, and 20th cycles.

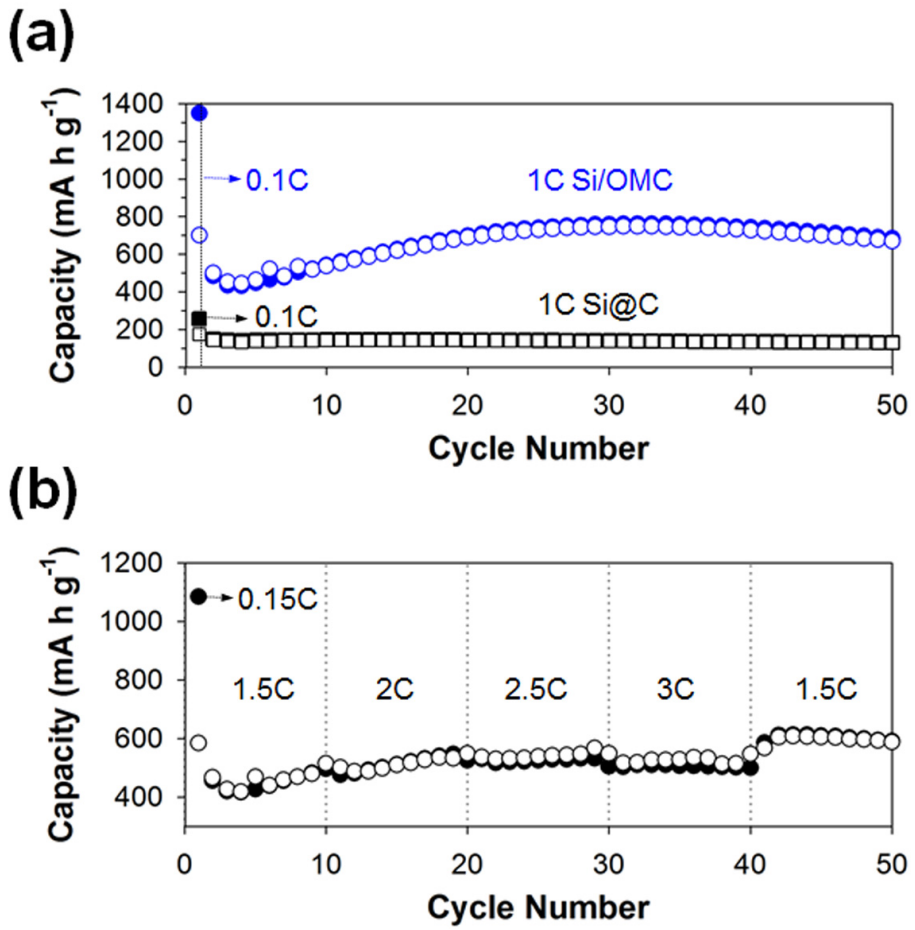

Figure 2-11 (a) Comparison of the cycling performance of the Si/OMC composite and the Si@C composite. (b) Rate capability of the Si/OMC composite.

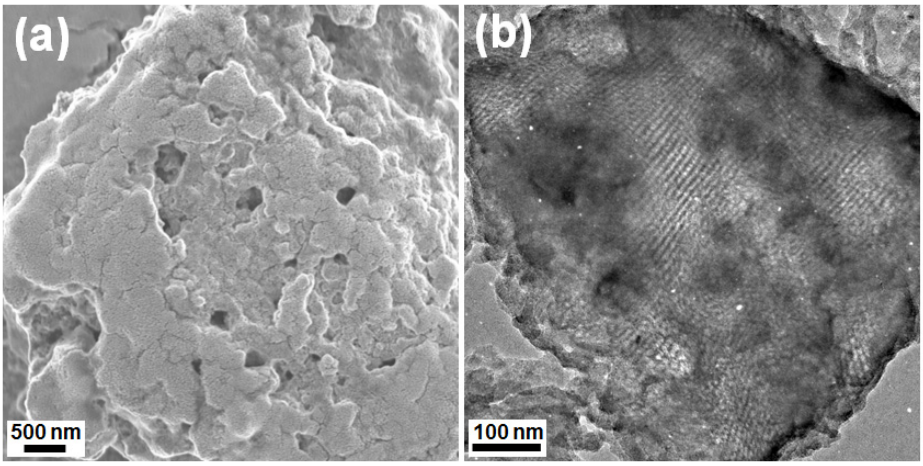

Figure 2-12 (a) SEM image and (b) HR-TEM image of Si/OMC composite after the cycling.

Chapter 3. Co_3O_4 nanoparticles Embedded in Ordered Mesoporous Carbon with Enhanced Performance as Anode Material for Li-ion Batteries

3.1 Introduction

The development of Li-ion batteries with a high energy density, high-rate capability and excellent cycling performance are urgently demanded for use in areas that include electric vehicles, portable electronics, and renewable energy sources. New electrode materials with high specific capacities are needed to meet these demands. Transition metal oxides have attractive electrochemical lithium storage capabilities [49,50]. Among this class of metal oxides, cobalt oxides have been widely studied as anode materials for use in high performance Li-ion batteries due to their high theoretical capacity of 890 mA h g^{-1}, which is more than twice that of the currently available commercial graphite (372 mA h g^{-1}) [51]. However, cobalt oxides have problems, including a large volume expansion during Li insertion/extraction and poor electrical conductivity. In order to overcome these problems, several studies focused on the possibility of hybridizing cobalt oxide nanoparticles (NPs) with electrical conducting metrics [52,53]. Carbon metrics e.g., amorphous carbon, [54,55] carbon nanotubes, [56] or

graphene sheets [57-59] can serve as structural buffers to effectively accommodate the strain caused by the volume change of cobalt oxides and ensure electrical connectivity during the charge/discharge process. In addition to these advantages over a carbon metric, ordered mesoporous carbon (OMC) has well-defined ordered mesochannels which can shorten the Li ion diffusion path from/to the bulk electrolyte phase, which leads to high specific capacities. Cobalt oxides NPs loaded in ordered mesochannels of OMC have been recently reported that an impregnation method with CMK-3 was used [30]. However, the preparation of a cobalt oxides/OMC nanocomposite based on the CMK-3 is a multi-step process, including repeated impregnation with carbon and metal precursors and the removal of hard templates, which is both time and energy consuming. The other carbon metrics mentioned above are not suitable for the large-scale manufacturing process due to the production of hazardous pollutants (e.g. strong acid), costs and multiple production processes. For an industrial application, a facile, scalable, and one-pot synthesis of transition metal oxide/OMC nanocomposite is needed.

Here we report on a facile method for the preparation of Co_3O_4 NPs embedded in the OMC (Co_3O_4/OMC), in which Co_3O_4 NPs with an average size of only about 10 nm are homogeneously embedded in the OMC framework. The cobalt oxides/OMC composite was prepared *via* the solvent evaporation method induced by co-self-assembly strategy [60]. The OMC not only acts as a structural buffer to effectively accommodate the strain induced by the volume change of Co_3O_4 NPs during Li insertion/extraction,

but also provides a pathway for the rapid transport of Li ions. The Co_3O_4/OMC composite have several advantages, compared to other carbon metrics. These include low-cost, one-pot production, and the potential for large-scale production, as has been verified by a recent report on the preparation of OMC on a kilogram scale [61]. When tested as anode materials for Li ion batteries, the as-prepared Co_3O_4/OMC composite showed a very high reversible capacity as well as excellent cycling performance (~1025 mA h g^{-1} after the 100th cycle at a current density of 0.1 A g^{-1}).

3.2 Experimental

3.2.1 Preparation of Co_3O_4/OMC composite

All chemicals used in these experiments were purchased from Sigma-Aldrich, and were used without further purification. In a typical synthesis, resol precursors were prepared using phenol and formaldehyde in a base-catalyzed process according to a previous report [34]. Phenol (3.05 g) was melted at 40-42°C, then a sodium hydroxide aqueous solution (0.13g, 20 wt%) was added under stirring. After 10 min, formalin (3.15 g) was added dropwise, and the mixture was further stirring for 1 h at 70-75°C. Upon cooling to room temperature, the pH was adjusted with 0.5 M HCl solution until it reached a value of ~7.0. Water was then removed by vacuum evaporation at 50°C. The resol precursor was dissolved in ethanol.

F127 (1.02 g) and phenolic resol (3 mL) were dissolved in ethanol and $Co(NO_3)_2 \cdot 6H_2O$ (4 g) was then added to the solution. After stirring for 10 min, the homogeneous solution was poured into dishes to allow the ethanol to evaporate at room temperature, followed by heating in an oven at 120°C for 24 h. The product was calcinated at 700°C at a ramping rate of 1°C min^{-1} for 3 h under an Ar atmosphere and then annealed at 270°C in air for 3 h. A thermogravimetric (TGA) analysis of the Co_3O_4/OMC composite revealed that the weight content of Co_3O_4 in the composites was around 36.2% (Figure 3-1). Co_3O_4 NPs and Co_3O_4@C were also prepared for use in comparing the electrochemical performance. For the preparation of Co_3O_4 NPs, D.I. water (12.5 ml) and concentrated ammonia (12.5 ml, 28 wt%)

were mixed for 10 min and an aqueous $Co(NO_3)_4$ solution (5 ml, 1 M) was then added. After stirring for 30 min, the solution was transferred to a Teflon-lined autoclave and heated at 180°C for 24 h. The precipitates were washed with D.I. water and ethanol (Figure 3-2) [62]. The Co_3O_4 NPs coated with carbon was synthesized following the same preparation procedure as for the Co_3O_4/OMC composites without the presence of F127 (Figure 3-3).

3.2.2 Characterization of Co_3O_4/OMC composite

The morphologies of the Co_3O_4/OMC composite were observed by transmission electron microscopy (TEM, Jeol JEM-3010 with an accelerating voltage of 300 kV). X-ray diffraction patterns were recorded on a M18XHF-SRA diffractometer (MAC Science) operated at 50 kV and 100 mA with Cu *Kα* radiation (λ=1.5406Å). X-ray diffraction was carried out at room temperautere under an atmosphere of air. Nitrogen adsorption–desorption isotherms were obtained at 77K using an ASAP 2010 (Micromeritics) instrument. Pore-size distributions were determined by the BJH (Barret–Joyner–Hallender) method applied to the adsorption branches of the isotherms. Thermal analyses were carried out in a thermogravimetric analyzer (TGA, Versa Therm, Thermo Scientific). Approximately 1 mg of powdered sample was heated in air (100 mL min^{-1}). X-Ray photoelectron spectroscopy (XPS, AXIS–His, KRATOS) measurements were performed in a UHV chamber (base pressure ~ 5 X 10^{-10} Torr) equipped with a monochromatic Al Kα X-ray source operated at 15 kV and 450 W, and a hemispherical energy analyser. C 1s, O 1s, and Co 2p spectra were

composed of several component peaks, respectively, as represented by a mixture of Gaussian and Lorentzian functions on a Shirley-type background. The samples were prepared by sticking a thin layer of powder on a double sided carbon tape. The electrochemical performance of the Co_3O_4/OMC composites was evaluated by galvanostatic cycling and cyclic voltammetry. Coin-type cell (2032) was assembled with the Co_3O_4/OMC composite electrode as the working electrode, metallic Li as the counter and reference electrodes, 1 mol L^{-1} $LiPF_6$ dissolved in a mixture of ethylene carbonate (EC) and dimethyl carbonate (DMC)(1:1 by volume) as the electrolyte in an argon-filled glove box. The working electrode was composed of Co_3O_4/OMC composite (75 wt%), carbon black (10 wt%) and polyvinylidene fluoride (15 wt%). The charge/discharge cycles were measured at a 100 mA g^{-1} rate between 0.01 and 3.0 V versus Li/Li^+ using a battery tester (WBCS3000, Wonatech). The test cell was dissembled in a glove box for characterization of the morphology of the material after the cycling test. The working electrode was sonicated with DMC for 30 min and the powder material scraped off the Cu foil was analyzed by HR-TEM.

3.3 Results and discussion

The Co_3O_4/OMC composite is prepared by the co-assembly of phenolic resol, a triblock copolymer F127, and $Co(NO_3)_2 \cdot 6H_2O$, followed by carbonization and oxidation. Figure 3-4 illustrates the preparation of the Co_3O_4/OMC composites. $Co(NO_3)_2 \cdot 6H_2O$ is dissolved in an ethanol solution containing the phenolic resol and F127 (Figure 3-4(a)). Liquid crystal phases of a transition metal nitrate salt/triblock copolymer can be formed by hydrogen bonding between the ethylene oxide units of the triblock polymer F127 and $[Co(H_2O)_x]^{2+}$[63]. Evaporation of the ethanol drives the resol-F127-Co^{2+}composites into ordered liquid crystalline mesophases containing Co^{2+} in the form of an inorganic salt at room temperature (Figure 3-4(b)). Liquid crystalline mesophases are solidified by the cross-linking of resols, which can be easily induced by a thermopolymerization at 120°C [34]. The Co^{2+} ions are homogenously distributed into the ethylene oxide units of the ordered mesophases. The product is calcined at 700 °C in an Ar atmosphere (Figure 3-4(c)). The templates are removed and ordered polymers are transformed into homologous carbon frameworks during the calcinations process [34]. Co NPs are prepared by thermal decomposition of a Co^{2+} inorganic salt dispersed in the framework. The Co NPs are then oxidized to produce Co_3O_4 NPs via annealing at 250°C in air (Figure 3-4(d)).

TEM images of the Co_3O_4/OMC composite are shown in Figure 3-5. The ordered mesoporous carbon and well-dispersed Co_3O_4 NPs are obviously observed. As shown in Figure 3-5(a), uniform and small Co_3O_4 NPs with sizes

of less than about 10 nm are embedded in the wall of the OMC due to thermal decomposition and confinement in the polymeric framework [64]. The co-assembly process involving cobalt nitrate and resol results in the cross-linking of resol with a polycarboxylate chelated to Co^{2+} ions. The subsequent *in situ* carbonthermal reduction and oxidation leads to the generation of Co_3O_4 NPs embedded in the pore walls of the mesoporous carbon matrix [65]. HR-TEM images of Co_3O_4/OMC composite provide the evidence to support this explanation. Co_3O_4 NPs arranged along with pore wall can be identified because Co_3O_4 NPs were generated in the wall of the OMC (Figure 3-5(b)). The lattice fringes of the (220) plane corresponding to a *d* spacing of 2.9Å for the Co_3O_4 phase are observed. Figure 3-5(c) clearly shows Co_3O_4 NPs (black sphere) are not located inside of pore (white parts) but confined inside the pore walls (dark parts). The XRD patterns of Co_3O_4/OMC composite indicate that a crystalline Co_3O_4 phase with a face-centered-cubic (*Fd3m*) structure (JCPDS card no. 78-1970) is formed, as shown in Figure 3-6(a). No peaks corresponding to elemental Co were observed, indicating that the elemental Co phase had been completely converted to Co_3O_4. Phase. An additional diffraction peak at about 26.5° can be indexed into the (002) reflections of carbon phase [39]. These results show that the Co_3O_4/OMC composite consists of a crystalline Co_3O_4 phase and an amorphous carbon phase. The nitrogen adsorption/desorption isotherms and the pore size distribution plots of the Co_3O_4/OMC composite are shown in Figure 3-6(b) and (c), respectively. The OMC revealed a type IV isotherm with an H2 hysteresis loop, indicating the existence of uniform mesoporosity (Figure 3-6(b)). However, the

Co_3O_4/OMC composite exhibited a type IV isotherm with an H3 hysteresis loop. This is because macropores were formed by the large Co_3O_4 aggregates on the outer surface of the OMC, as evidenced by an increase in the pore size distribution [66]. Compared with about 5 nm uniform pores for the OMC, mesopores with diameters of 5 nm are decreased and micropores are increased in the Co_3O_4/OMC, which can be attributed to the formation of Co_3O_4 NPs inside the pore walls of the OMC (Figure 3-6(b)). The Brunauer-Emmett-Teller (BET) surface area (602.0 m^2 g^{-1}) and pore volume (0.45 cm^3 g^{-1}) for the OMC was decreased compared to those for the Co_3O_4/OMC composite (464.7 m^2 g^{-1} and 0.31 cm^3 g^{-1}, respectively) due to the blockage of mesopores by Co_3O_4 NPs. Figure 3-7 shows XPS spectra for the Co/OMC composite and Co_3O_4/OMC composite prepared by the annealing in air. Figure 3-7(a) exhibits the C 1s peak, which was resolved into three peaks corresponding to adventitious carbon, C-O, and O-C=O at 284.8 eV, 286.3 eV, and 288.6 eV, respectively [67-69]. The weaker C 1s peak after annealing in air indicates the oxygenation of the OMC. The O 1s spectra of the Co/OMC composite can be deconvoluted into two peaks, centered at 531.2, and 533 eV, generally attributed to oxide defect states, and surface hydroxylation (Figure 3-7(b)) [70]. After the annealing in air, a new peak at 529.4 eV, assigned to intrinsic O^{2-} ions forming oxides with cobalt, is appeared in O 1s peak. Figure 3-7(c) shows the Co 2p signals of the Co/OMC composite and Co_3O_4/OMC composite. After the annealing in air, the Co_3O_4/OMC composite displays a characteristic sharpening of the main 2 $p_{3/2}$ at 779.8 eV and 2 $p_{1/2}$ peaks at 795.2 eV. And intensity of the satellite structure of the octahedral Co^{2+} cation,

circled in Fig. 2c, was decreased [70]. The sharper Co 2p XPS peaks and the diminished satellite intensity show the formation of Co_3O_4 phase.

The electrochemical properties of Co_3O_4/OMC composite were examined by cyclic voltammetry and galvanostatic cycling analyses. Figure 3-8(a) shows charge/discharge profiles for the pure Co_3O_4 NPs and Co_3O_4/OMC composite electrode at a current density of 0.1 A g^{-1} in the voltage range of 0.01 and 3.0 V vs. Li/Li^+. In the first negative scan, the pure Co_3O_4 electrode exhibits a long plateau at 1.0 V vs. Li/Li^+, with a discharge capacity of around 1082 mA h g^{-1}. However, after 50 cycles, the reversible capacity dramatically decays to 55 mA h g^{-1}. The redox reaction of Co_3O_4 differs from the classical mechanism (reversible insertion/deinsertion of lithium or a lithium alloying reaction). The overall redox reaction can be expressed as follows:[71]

$Co_3O_4 + 8Li \leftrightarrow 3Co + 4Li_2O$

In the first discharge process, Co_3O_4 undergoes decomposition to give metallic Co nanograins that are embedded in a Li_2O matrix. Upon the following charge process, the Co is reoxidized into nanosized Co_3O_4 and Li_2O are decomposed. Confinement of the metallic Co in an amorphous Li_2O matrix can induce an internal loss of electrical contact and the irreversible reduction of Li_2O because Li_2O is an electrochemically inactive phase [72,73]. Therefore, the continuous accumulation of Li_2O leads to the loss of electrical contact, resulting in capacity fading of the Co_3O_4 electrode in subsequent charge/discharge cycling [74]. The Co_3O_4/OMC composite electrode display a better cycling performance than that for the pure Co_3O_4 electrode. The Co_3O_4/OMC composite exhibits a discharge capacity of 1515 mA h g^{-1} and a

charge capacity of 995 mA h g^{-1} in the first cycle. The coulombic efficiency was 66% for the first cycle. The irreversible capacity can be attributed to the incomplete conversion reaction and irreversible lithium loss due to the formation of an SEI layer [75]. After the second cycle, the Co_3O_4/OMC composite electrode shows a stable cyclability and retains a high reversible capacity of 968 mA h g^{-1} after 50 cycles. Figure 3-8(b) represents the differential capacity plots of the first and second charge/discharge for Co_3O_4/OMC composite. In the first discharge, three peaks at 1.5, 1.03 and 0.82 V and broad peak below 0.6 V are appeared. The small peak at 1.5 V may be related to the insertion of Li ions into Co_3O_4 leading to $Li_xCo_3O_4$ [76]. The reduction peak with a maximum at 1.03 V is assigned to the electrochemical lithiation of Co_3O_4 NPs embedded in the OMC. Once the discharge potential reaches around 1.1 V, metallic Co and Li_2O are formed via the reduction of the Co_3O_4 [77]. The shoulder peak at 0.82 V and the broad peak with an onset potential of 0.6 V represent the intercalation reaction of Li ions with the OMC and the formation of a SEI [78]. The main peak shifts to 1.2 V in the second cycle due to the structural change and the interfacial property of Co_3O_4 phase. In the oxidation scan, the two charge peaks appear at around 1.2 and 2.05 V. These corresponded to the reverse processes in which Co is reoxidised to Co_3O_4 and the decomposition of Li_2O [79]. As shown in Figure 3-8(c), the cycling behaviour of the Co_3O_4/OMC composite, the pure Co_3O_4 NPs and the OMC and the Co_3O_4/OMC composite electrode were compared for a total of 100 cycles. The Co_3O_4/OMC composite reaches a Coulomic efficiency of more than 98% within four cycles. The reversible

capacity of the Co_3O_4/OMC composite increases slightly with cycling and finally reaches 1025 mA h g^{-1} after 100 cycles. The high capacities of the Co_3O_4/OMC composite are related to the increased charge storage within the polymeric surface layer [80-82]. In the first discharge, Co_3O_4 NPs are converted into metallic Co nanograins that are embedded in a Li_2O matrix coated with a SEI layer. The outer layer is surrounded by an electrochemically active polymer/gel-like coating. The polymer coating binds tightly to the Co NPs, ensuring an electronic conducting path between the Co NPs and catalytically enhances electrolyte reduction [77]. The gradual increase in capacity over the 60 cycles can be explained by this phenomena. Not all surfaces of the Co_3O_4 NPs embedded deeply inside pores of the OMC are covered with a polymer layer on the first discharge. This occurs slowly over several cycles and the polymer layer that forms on the surfaces of all Co_3O_4 NPs causes them to be located within the pores of the Co_3O_4/OMC composite. To investigate this phenomenon, a TEM image of Co_3O_4/OMC composite after cycling test was analyzed (Figure 3-9). Increased size of Co_3O_4 NPs embedded in the carbon framework by the conversion reaction with Li-ion can be identified. However, a detailed investigation of the internal pores was difficult due to the thick SEI formed on the surface of the composite. Figure 3-8(d) exhibits rate capabilities of the Co_3O_4/OMC composite operated at various rates from 0.05 to 1.5 A g^{-1}. Highly stable reversible capacities of around 1130, 1000, 870, 800, 720, 660, and 580 mA h g^{-1} were obtained at current densities of 0.05, 0.1, 0.5, 0.7, 1.0, 1.2, and 1.5 A g^{-1}, respectively. When the rate returns to the initial 0.05 A g^{-1} after cycling at 1.5 A g^{-1}, the

electrode recovers its original capacity even slightly higher (1148 mA h g^{-1} for the 40th cycle). The stable rate capability of the Co_3O_4/OMC composite can be induced by the unique structure, which ensures the formation of enlarged active sites for electrochemical reactions with cylindrical mesochannels of the OMC which facilitates the diffusion of Li ions of the electrolyte. This property is useful when the battery is discharged or charged at a high current. To further understand the effect of the mesopores on the diffusion of Li ions, the Li diffusion coefficient in the Co_3O_4/OMC composite electrode and Co_3O_4 NPs coated with non-porous carbon (Co_3O_4@C) electrode at room temperature were compared. Figure 3-10(a) shows cyclic voltammograms for the Co_3O_4/OMC composite with different scan rates from 0.1 to 1.0 mV s^{-1}. The height and area of the cathodic and anodic peaks increase with increasing scan rate. The voltammetric peaks during the polarization of the cell can be used to calculate the apparent diffusion coefficient of Li ions. As shown in Figure 3-10(b), the current density (i_p) is proportional to the square root of the scan rate ($v^{1/2}$). If the rate of electron transfer is fast at the electrode surface and the restraining process is the diffusion of Li in the electrode, the i_p for which can be expressed as:[83]

$$i_p = \left(2.69 \times 10^5\right) n^{3/2} A D_{Li^+}^{1/2} C_{Li^+}^{*} \nu^{1/2}$$

where i_p is the peak current value, n is the number of electrons involved in the reaction of the redox couple, C_{Li} is the bulk concentration of Li in the electrode (mol cm^{-3}), A is the apparent contact area between the electrode and electrolyte (cm^2), ν is the rate at which the potential is swept (V s^{-1}), D_{Li} is the

apparent diffusion coefficient ($cm^2\ s^{-1}$). Calculated from the slope of the linear fit, the apparent diffusion coefficients for the Co_3O_4/OMC composite is $4.1\times10^{-11}\ cm^2\ s^{-1}$. This value is higher than that of Co_3O_4@C composite, where D_{Li} is $1.6\times10^{-11}\ cm^2\ s^{-1}$ (Figure 3-11). This result indicates that the mesoporous structure of the OMC facilitates the transport of Li ions during cycling.

These results demonstrate that the Co_3O_4/OMC composite achieves an enhanced cycling stability and rate capability as an anode material in Li ion batteries due to its unique mesoporous nanostructure. First, the mesopores in the OMC not only provide pathways for efficient Li ion transport but also accommodate the volumetric expansion and shrinkage of Co_3O_4 during lithiation/delithiation cycling. Second, the Co_3O_4 NPs that are homogeneously distributed in the pore wall of the OMC prevent aggregation and pulverization during cycling and minimize the risk of side reactions.

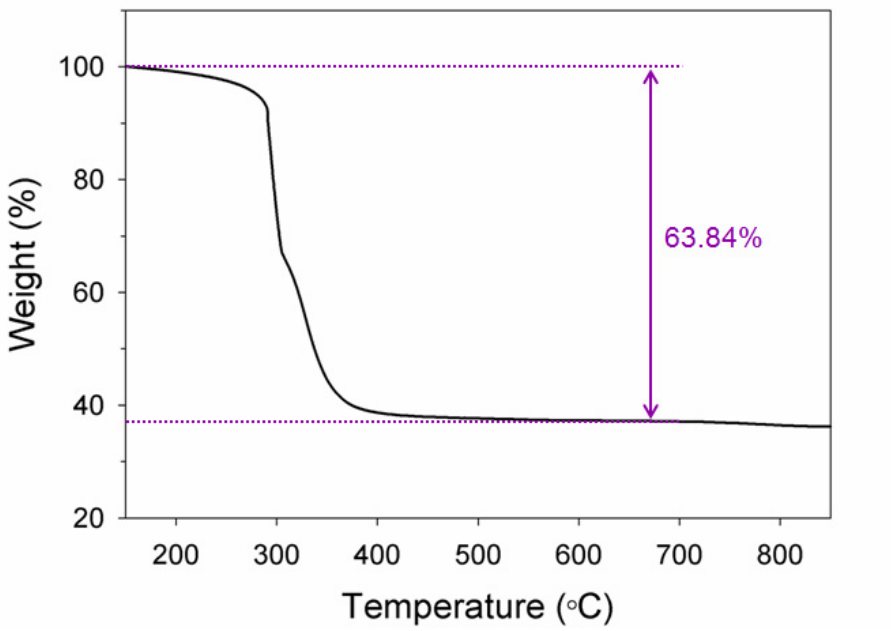

Figure 3-1 TGA analysis of the Co_3O_4/OMC composite.

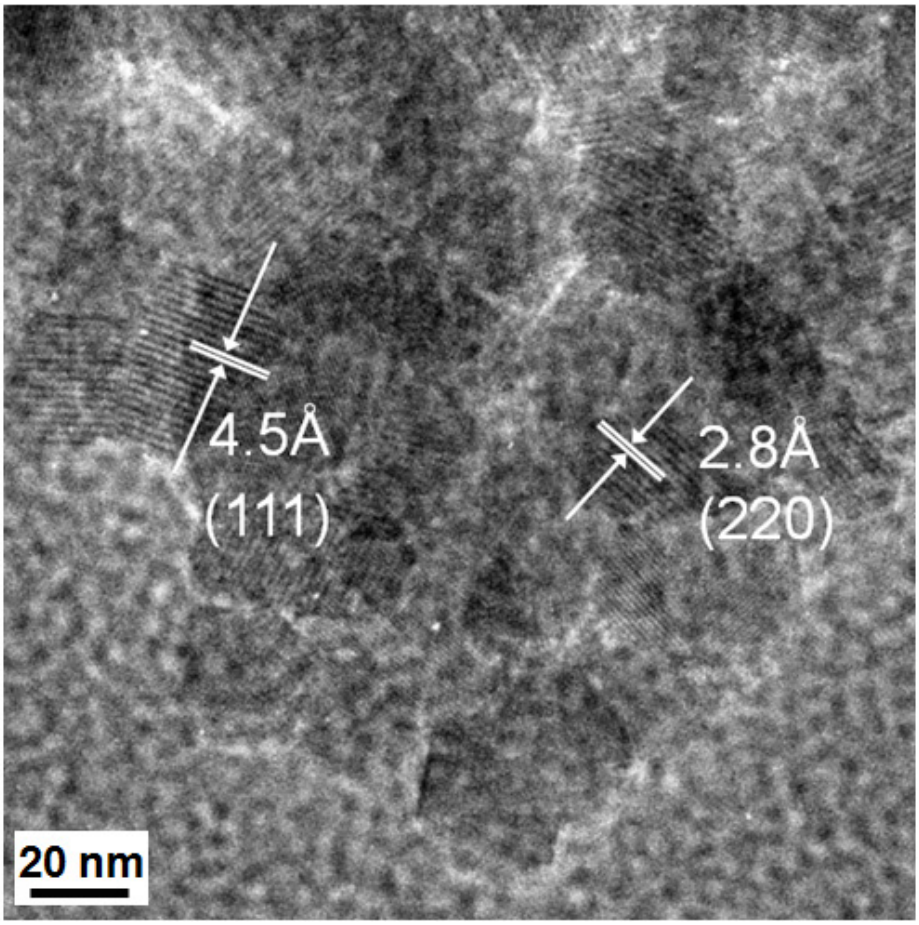

Figure 3-2 HR-TEM images of the homemade Co_3O_4 NPs.

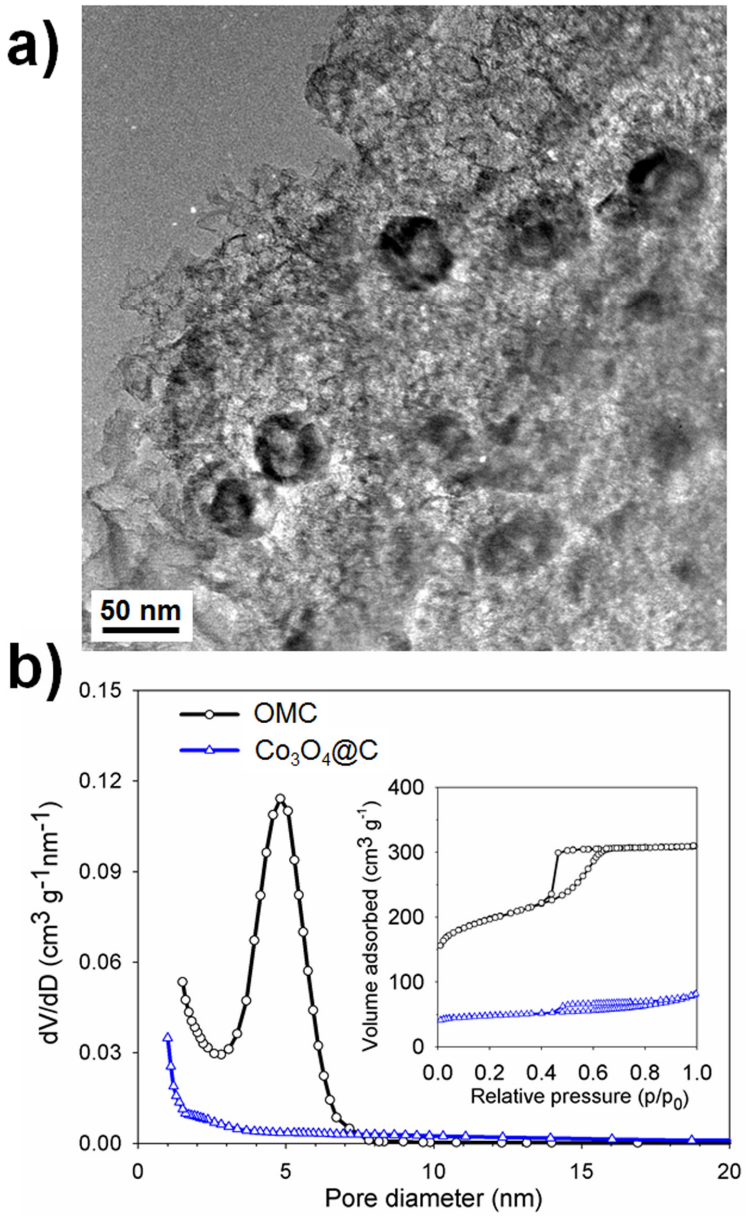

Figure 3-3 a) HR-TEM images of the Co_3O_4@C composite. b) Pore size distribution and nitrogen adsorption-desorption isotherm (inset) of OMC and Co_3O_4 @C composite

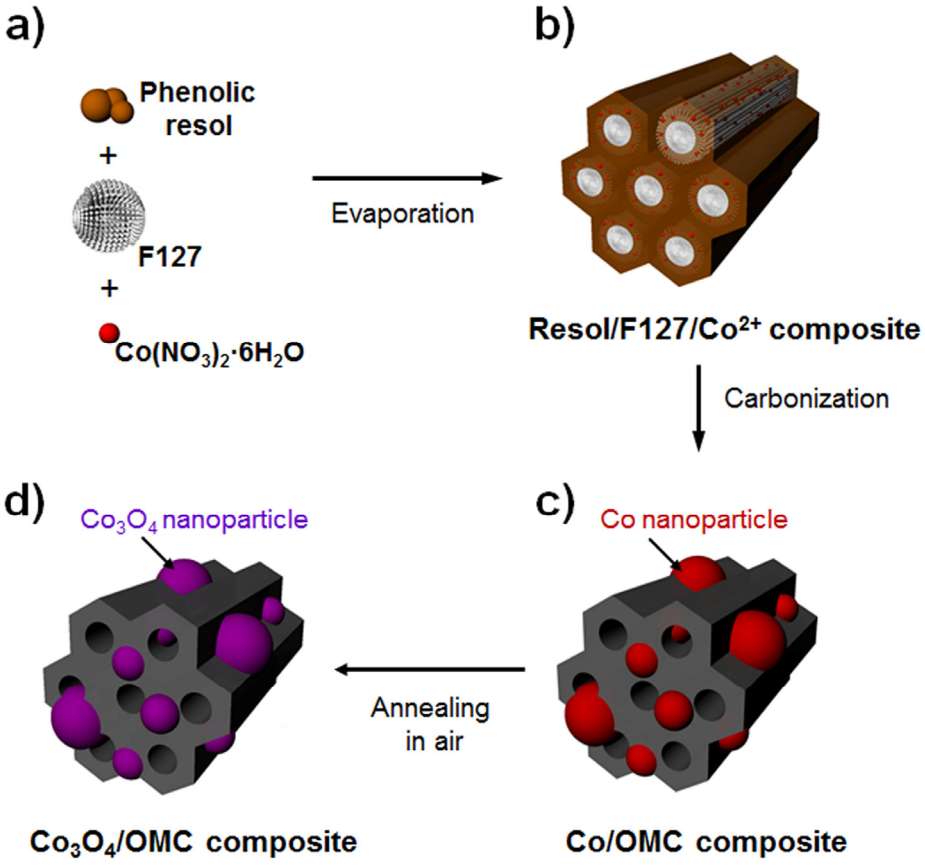

Figure 3-4 Schematic representation of the procedure used in the preparation of the Co_3O_4/OMC composite.

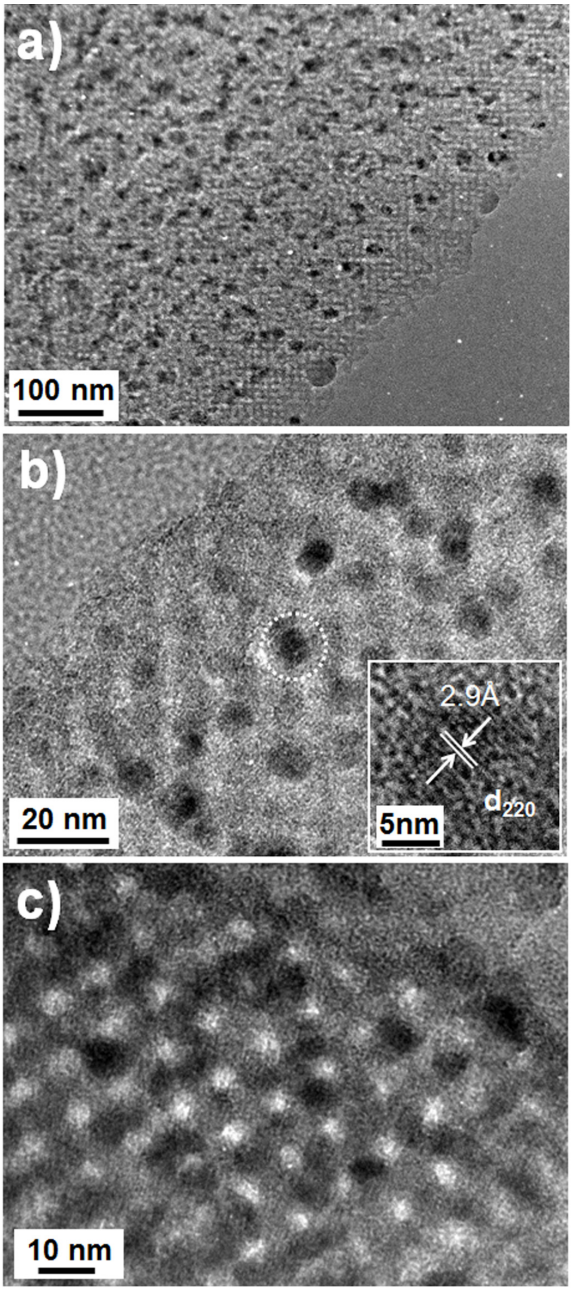

Figure 3-5 (a,b,c) High-resolution transmission electron microscopy images of Co_3O_4/OMC composite.

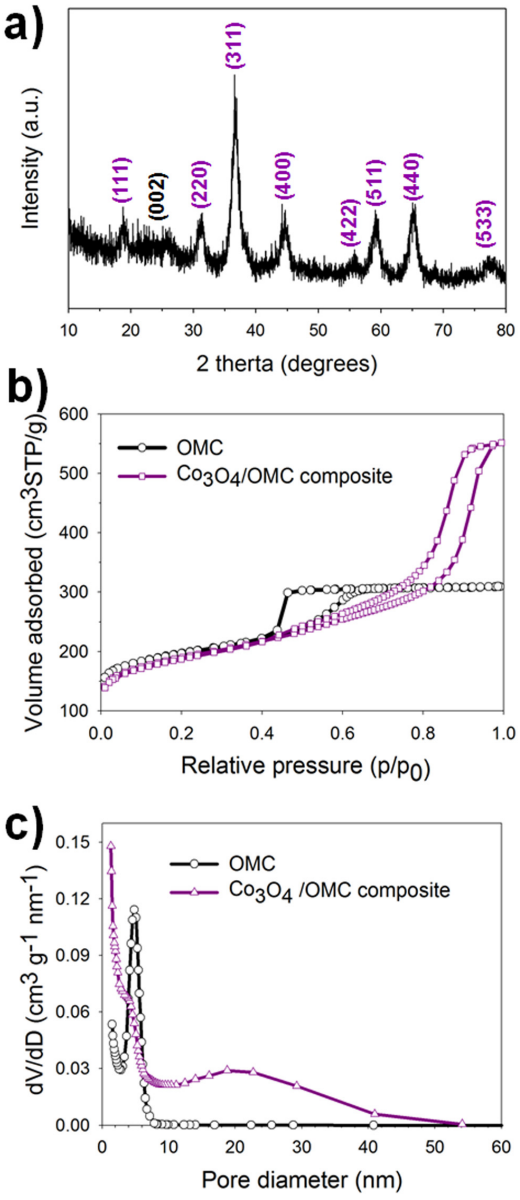

Figure 3-6 (a) XRD patterns of Co_3O_4/OMC composite. (b) Nitrogen adsorption-desorption isotherm and (c) pore size distribution of OMC and Co_3O_4/OMC composite

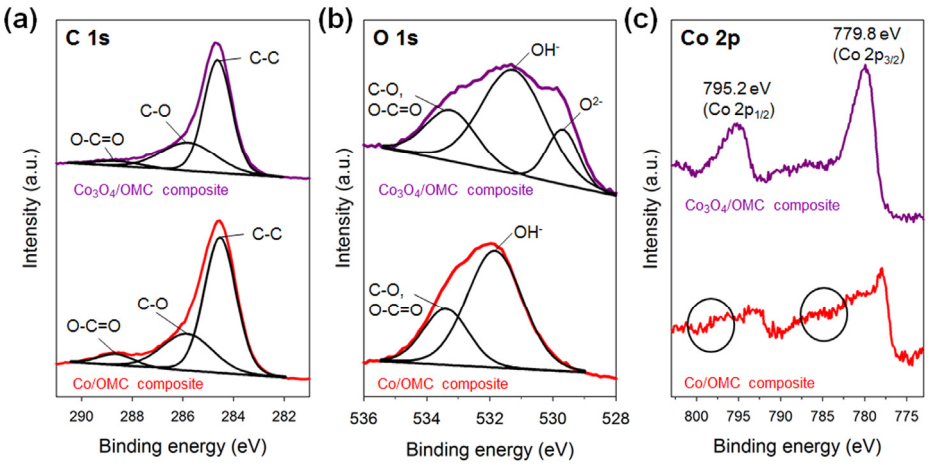

Figure 3-7 XPS spectra of a) C 1s, b) O 1s, c) Co 2p regions of Co/OMC composite and Co_3O_4/OMC composite.

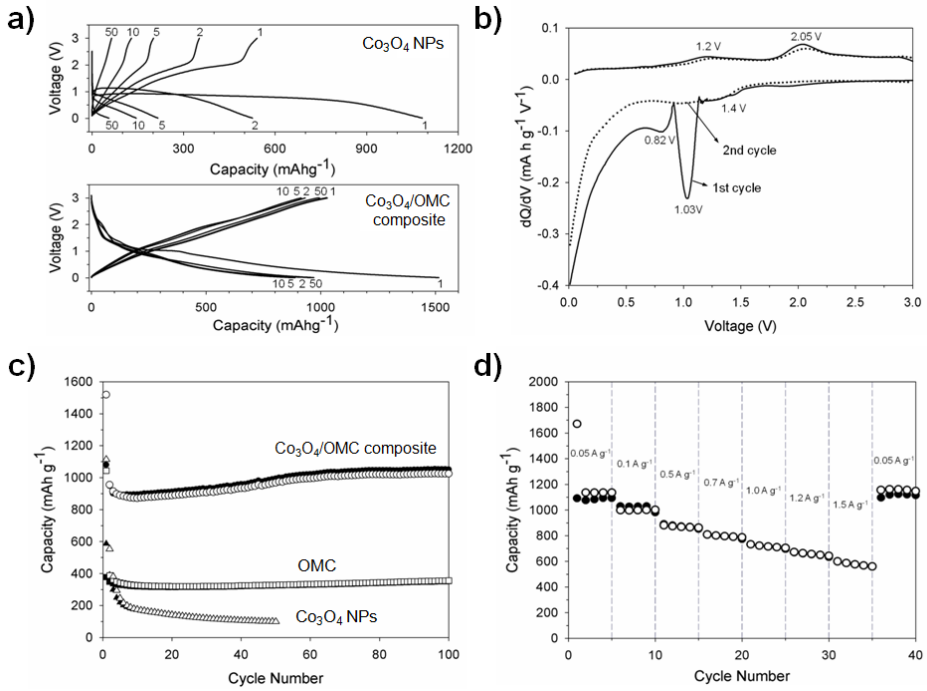

Figure 3-8 (a) Galvanostatic charge-discharge profiles of the Co_3O_4 NPs electrode (upper) and Co_3O_4/OMC composite electrode (downward) between 0.01 and 3 V vs Li/Li^+ for the 1st, 2nd, 5th, 10th and 50th cycles at a rate of 0.1 A g^{-1}. (b) Differential capacity curves of the first and second cycle of the composite electrode. (c) Comparison of the cycling performance of the Co_3O_4/OMC composite, OMC, and pure Co_3O_4 NPs electrodes cycled at a rate of 0.1 A g^{-1}. (d) Rate capability of the Co_3O_4/OMC composite at different rates from 0.05 to 1.5 A g^{-1}. All electrochemical measurements were carried out at room temperature in two-electrode 2032 coin-type half cells.

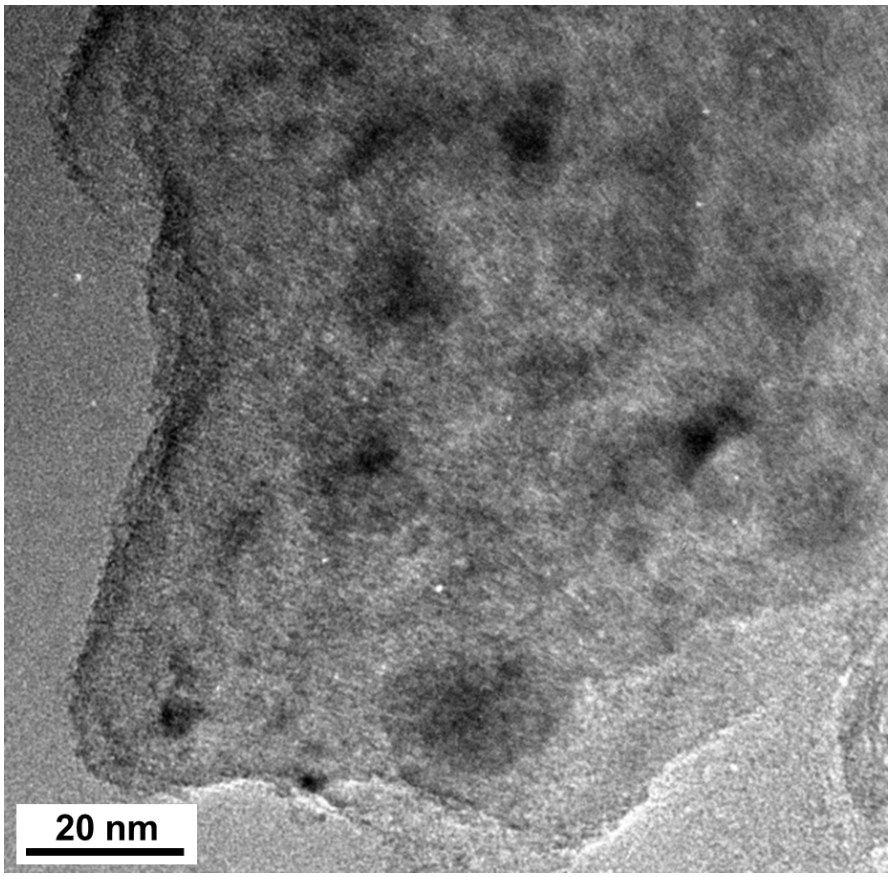

Figure 3-9 High-resolution transmission electron microscopy images of Co_3O_4/OMC composite after cycling test.

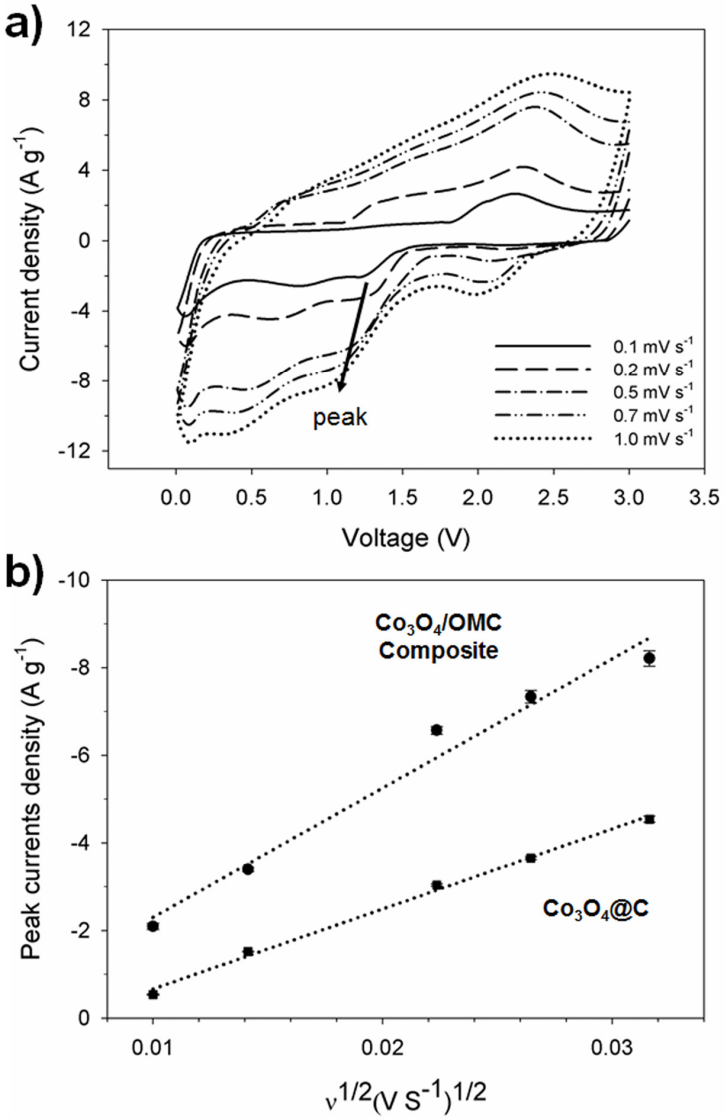

Figure 3-10 (a) Cyclic voltammetry curves of the Co_3O_4/OMC composite with different scan rates from 0.1 to 1.0 mV s^{-1}. (b) The relationship of the peak current (i_p) and the square root of scan rate ($v^{1/2}$) of the Co_3O_4/OMC composite and Co_3O_4@C composite.

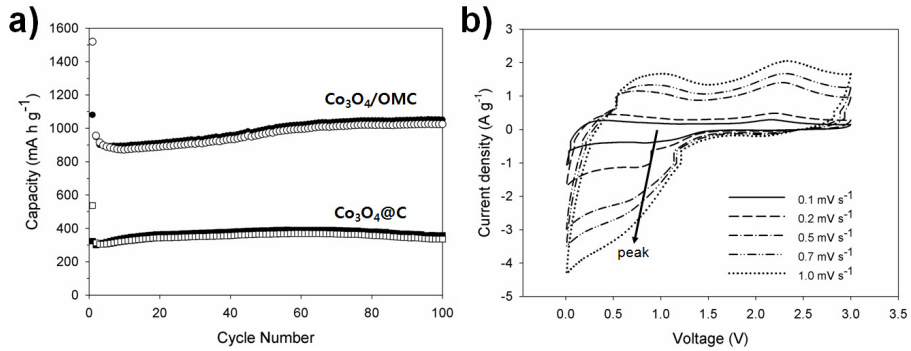

Figure 3-11 (a) Comparison of the cycling performance of the Co_3O_4/OMC composite and Co_3O_4@C composite electrodes cycled at a rate of 0.1 A g^{-1}. (b) Cyclic voltammetry curves of the Co_3O_4@C composite electrode with different scan rate: 0.1, 0.2, 0.5, 0.7 and 1.0 mV s^{-1}

Chapter 4. Synthesis of Three Dimensional Co_3O_4 Composites based on Aligned Mesoporous Carbon Nanotube for Li-ion Battery Anode Applications

4.1 Introduction

Nano-size transition metal oxides are considered to be promising anode materials for use in Li-ion batteries [49]. Among these oxides, Co_3O_4 was reported to show a high theoretic reversible specific capacity of 890 mA h g^{-1} [50]. However, the low electrical conductivity and large volume change that occurs during charge/discharge cycling result in poor capacity retention. In order to overcome these problems, hybridizing Co_3O_4 nanoparticles (NPs) with conducting matrices with different morphological structures represents a potentially effective solution to the problem [84]. Moreover, three-dimensional (3-D) structured electrodes have also recently attracted considerable interest for effectively increasing energy density and high-rate discharge capabilities because such 3-D architectures not only increase the amount of active material within a given footprint area but also shorten the diffusion length path of Li ions [85]. In addition, a 3-D mesoporous nanotube in which the mesoporous structure is combined with a 1-D morphology is rather fascinating because the interconnected pore network would facilitate assess of the electrolyte to the interior of the MCNT [4, 86].

In view of the 3-D nanostructured electrode design, hybridizing Co_3O_4 NPs with a mesoporous carbon nanotube is attractive because the carbon framework acts as a highly conductive current collector and the inner pore volume provides an efficient void space to buffer the volume expansion that occurs during the reaction and the porosity serves as a pathway for continuous electrolyte transport.

In this study, we report on the synthesis of 3-D mesoporous carbon nanotubes (MCNT) filled with Co_3O_4 NPs (Co_3O_4/MCNT) aligned directly onto a current collector (Cu) as an anode electrode for Li-ion batteries. The Co_3O_4/MCNT was prepared by the co-self-assembly of Pluronic F127, a resorcinol-formaldehyde polymer and $Co(NO_3)_2$ in the pores of the anodic aluminum oxide (AAO) membrane. The resulting electrode showed an enhanced electrochemical performance attributed to the three-dimensional structure of the MCNT framework filled with well-dispersed small Co_3O_4 nanoparticles.

4.2 Experimental

4.2.1 Preparation of Co_3O_4/MCNT electrode

The Co_3O_4/MCNT electrode was prepared by the co-self-assembly of a phenol resol, Pluronic F127 and $Co(NO_3)_2 \cdot 6H_2O$ in the pores of the AAO template, followed by carbonization, oxidation, and etching of the AAO template. The phenolic resol precursor was prepared by polymerizing 0.61 g of phenol and 1.05 g of formaldehyde (37 wt%) containing 0.39 g of formalin by a base-catalyzed process, following a previously described procedure [34]. A 0.34 g sample of the triblock copolymer F127 was dissolved in 10 mL of ethanol. A 1 mL aliquot of the resol precursor solution in ethanol was then added. After stirring for 30 min, a homogeneous solution was produced. A 1.2 g of $Co(NO_3)_2 \cdot 6H_2O$ was added to a stirred resol precursor and F127 in the ethanol for over a 30 min period. The homogeneous precursor sol infiltrated the channels of the AAO membrane (Anodisc^{TM}, Whatman) with average channel diameters of 100 nm and a thickness of approximately 60 μm. The precursor sol was converted into a gel during the evaporating of ethanol at ambient temperature and the resulting membrane was then heated in an oven at 120^{o}C for 4h. The composite membrane was calcined at 650^{o}C at a heating rate of 1 ^{o}C min^{-1} for 4 h under a stream of argon to decompose the surfactant molecules and carbonize the mesoporous walls. An oxidation was then performed in air at 270^{o}C for 3 h. The Cu thin film was deposited on the composite membrane by vacuum thermal evaporation using a high purity Cu pellet (99.999% pure, Materion) in a tungsten crucible. Before the evaporation, a pressure of about 8.0×10^{-4} Torr was reached in the chamber. The deposition rate was 5~10Å s^{-1}

and the final thickness of the film was 0.5 μm. A quartz crystal microbalance was employed to control the growth rate of the film. The Co_3O_4/MCNT electrode on the Cu thin film were released by an etching AAO template by immersing the sample in a 5 M H_3PO_4 aqueous solution for 10 h, followed by washing with deionized water and ethanol several times. To compare the electrochemical performance, MCNT, Co_3O_4/carbon nanotubes (CNT) and Co_3O_4 nanotubes (NT) were prepared by the same procedure without $Co(NO_3)_2$, F127 and phenolic resols, respectively.

4.2.2 Characterization of Co_3O_4/MCNT electrode

The Co_3O_4/MCNT electrode was characterized by field-emission scanning electron microscopy (SEM, Carl Zeiss, SUPRA-55VP) and high-resolution transmission electron microscopy (HR-TEM, Jeol, JEM-3010). Wide angle X-ray diffraction (XRD) patterns were obtained using a M18XHF-SRA diffractometer (MAC Science).

When the Co_3O_4/MCNT electrode is aligned directly onto the current collector, the use of conductive additives and binders are not needed. Electrochemical characterizations were performed using coin-type half cells (2032 type) prepared in argon-filled glove box that contained an electrode, Li metal foil (Alfa aesar) as both the reference and counter electrodes, a microporous polyethylene separator, and an electrolyte solution of 1 M $LiPF_6$ in 1:1 w/w ethylene carbonate: diethyl carbonate (Panax e-tec). The cells were discharged (Li-ion insertion) and charged (Li-ion extraction) at a current density of 100 mA g^{-1} in a voltage range from 0.01 to 3.0 V (vs. Li/Li^+) using a battery tester (WBCS3000, Wonatech). Electrochemical impedance spectroscopy (EIS, ZIVE SP2, Wonatech) measurements were

performed over a frequency rate of 200 kHz to 10 mHz at different charge-discharge stages by applying an AC signal of 5 mV. The electrical parameters in the equivalent circuit calculated using the ZIVE ZMAN 2.2 computer program.

4.3 Results and discussion

The Co_3O_4/MCNT electrode was prepared by a dual-template strategy, combining a hard-template and a soft-template, *via* a one-step co-self-assembly synthesis. The precursor sol was vigorously mixed with a phenol-formaldehyde resol as the carbon precursor, an amphiphilic surfactant, F127, was used as the soft template, and $Co(NO_3)_2 \cdot 6H_2O$ as the cobalt oxide precursor. A commercially available AAO membrane was used as a hard template (Figure 4-1(a)). The precursor sol infiltrated the pores of the AAO membrane. During the evaporation of ethanol at room temperature, the resol/F127/$Co(NO_2)_3$ composite was transformed into an ordered liquid crystalline mesophase in the channels of the AAO template by the self-assembly of block copolymers (F127). The self-assembly of the composite was essentially driven by hydrogen bonding interactions between the resol and the F127 [34]. The mesophase was subsequently converted into a solid by heating the preparation to 120 °C (Figure 4-1(b)). The carbonization was conducted by heating the AAO template infiltrated with the precursor gel at 650°C for 4h under a stream of Ar. Upon carbonization, the F127 soft template was removed by heating at 350°C and the polymers were transformed into carbon at 650°C. The Co_3O_4 NPs were prepared by thermal decomposition of Co^{2+} ions and annealing at 270°C in air. The Co_3O_4/MCNT composite embedded in the AAO template were directly assembled with a Cu thin film employed as a current collector by thermal evaporation under vacuum conditions (Figure 4-1(c)). To remove the AAO template, Co_3O_4/MCNT electrode embedded in the AAO template was allowed to stand in a 5 M H_3PO_4 solution for 10h (Figure 4-1(d)).

Figure 4-2 shows the SEM images and HR-TEM images of the Co_3O_4/MCNT electrode prepared by the dual-templating process. The lengths of the Co_3O_4/MCNT typically exceeded tens of micrometers. The strong interaction between the resin polymer and the inner wall surface of the AAO *via* hydrogen bonding result in the formation of a nanotube structure inside the AAO template during the high temperature carbonization [87]. Partial openings which exist on the outside wall of the MCNT confirm that the inside of the MCNT contains void spaces (Figure 4-2(a)). The surface of the Co_3O_4/MCNT is not smooth due to presence of the mesopore structure and the inside of the MCNT is filled with Co_3O_4 NPs (Figure 4-2(b)). The HR-TEM images show that the Co_3O_4 NPs are uniformly dispersed on the inside of the MCNT (Figure 4-2(c)). Bubble-like macropores on the outside of the MCNT can be formed from small air bubbles that were trapped in the AAO channels during the self-assembly process [87]. The Co_3O_4 NPs, which were uniformly dispersed on the inside of the MCNT, have an average diameter of about 10-20 nm, can be identified through the macropore on the outside wall of the MCNT (Figure 4-2(d)). However, the ordered mesoporous structure of the MCNT with the elliptical shaped mesopores cannot be identified (Figure 4-3). Figure 4-2(e) exhibits the XRD pattern of the Co_3O_4/MCNT composite raked out from the Cu thin film. The major diffraction peaks are in agreement with published values for Co_3O_4 with a face-centered-cubic (*Fd3m*) structure (JCPDS card no. 78-1970). An additional small and a low broad diffraction peak appears at around 2θ of 26° which correspond to the (002) plane of amorphous carbon [39].

The voltage profiles of the Co_3O_4/MCNT and Co_3O_4 NT electrode for

different cycles at a current density of 0.1 A g^{-1} are shown in Figure 4-4(a). The first discharge and charge capacities are 2147 and 1037 mA h g^{-1} for Co_3O_4/MCNT and 1284 and 683 mA h g^{-1} for Co_3O_4 NT. The initial capacity loss may result from an incomplete conversion reaction an irreversible lithium loss due to the formation of the SEI layer [75]. The high capacity particulate composite electrodes with porous morphologies undergo irreversible reactions following electrolyte exposure [88]. After the second cycle, the Co_3O_4/MCNT electrode shows a better electrochemical lithium storage performance and capacity retention than the Co_3O_4 NT electrode. These electrodes have different mechanical stabilities and electron conductivities by presence of carbon which provides a stable framework, resulting in efficient electron transport [27]. Figure 4-4(b) presents the differential capacity curves for the Co_3O_4/MCNT and Co_3O_4 NT electrodes measured during the first cycle. The reduction peaks (at 1.67 V and 2.01 V) and oxidation peak (at 0.92 V) and for Co_3O_4/MCNT electrodes and the reduction peaks (at 1.47 V and 2.07 V) and oxidation (at 1.0 V) for Co_3O_4 NT electrodes were observed, which are attributed to the reaction of Li with Co_3O_4 [77]. In addition, a broad oxidation peak appearing below 0.5V and at 1.65 V in the case of the Co_3O_4/MCNT electrodes was observed, which was absent in the case of the Co_3O_4 NT electrode. This peak is mainly the result of the formation of a SEI layer on the carbon surface and the insertion of lithium into the amorphous carbon, indicating that the carbon in the Co_3O_4/MCNT is also electroactive for Li storage [89]. Figure 4-4(c) shows the cycling behavior of the Co_3O_4/MCNT, Co_3O_4/CNT, and Co_3O_4 NT electrode. The Co_3O_4/MCNT electrode shows moderate capacity fading behavior in the first 10 cycles, followed by relatively flat and low capacity

fading behavior for the next 50 cycles with an irreversible capacity loss of less than 0.4% per cycle. The discharge capacity of the Co_3O_4/MCNT electrode remains at 627 mA h g^{-1} after 50 cycles. In contrast, in the case of the specific capacity of the Co_3O_4/CNT electrode, without a mesoporous structure, the Co_3O_4 NT electrode drops to 245 mA h g^{-1} and 70 mA h g^{-1}, respectively. Figure 4-4(d) shows the results for an evaluation of the rate performance of the Co_3O_4/MCNT at continuously variable rates from 0.2 to 1.0 A g^{-1}. The electrodes show an irreversible capacity loss during the first cycle at a current density of 0.2 A g^{-1} due to decomposition of the electrolyte and/or solvent. The reversible capacities are retained at ~ 338, 236, and 179 mA h g^{-1} at 0.5 and 0.7 and 1.0 A g^{-1}, respectively. After 20 cycles, with the current rate being decreased back to 0.2 A g^{-1} a capacity of ~393 mA h g^{-1} can be recovered for the Co_3O_4/MCNT.

In order to better understand the electrochemical performance of this system, electrochemical impedance spectra were obtained for Co_3O_4/MCNT and Co_3O_4/CNT. Figure 4-5(a) shows Nyquist plots of the electrodes in the high frequency range in the first cycle and after the tenth cycle (inset). The diameter of the semicircle for Co_3O_4/MCNT is smaller than that of Co_3O_4/CNT, indicating that good electronic contact was achieved. The equivalent circuit was built to qualitatively describe simple elements such as resistance, and capacitance of the electrode materials (Figure 4-6) [90]. The calculated data from the circuit model by fitting procedures yielded quantitative data (Table 4-1). The increase in the surface resistance (R_{sur}) is the effect of the formation on a SEI surface [91, 92]. After the first cycle, the value of R_{sur} for all electrodes shows a total increasing trend. However, No relevant changes in the Co_3O_4/MCNT electrode were observed between the

R_{sur} of the first and tenth cycle, compared with the Co_3O_4/CNT electrode. The reason for this is because the well dispersed small Co_3O_4 NPs in MCNT aids in the formation of a stable and dense SEI film [93-95]. The co-self-assembly process involving cobalt nitrate and resol results in the cross-linking of the resol with a polycarboxylate moiety that is chelated to Co^{2+} ions. The subsequent *in situ* carbonthermal reduction and oxidation leads to the generation of Co_3O_4 NPs embedded in the pore walls of the mesoporous carbon matrix [65]. Although the Co_3O_4/CNT electrode prepared without a soft template is coated with carbon, the Co_3O_4 NPs underwent aggregation without a confinement effect in the carbon framework, which may induce a large volume change during the electrode reactions (Figure S2). The repetitive decomposition and formation of a SEI film as the result of volume change may result in poor electronic contact [96]. Figure 4-5(b) shows a plot of the imaginary resistance determined by impedance spectroscopy as a function of the inverse square root of the angular frequency (ω) for an electrode. A linear behavior was observed for frequency values ranging from 0.2 Hz to 0.02 Hz with a slope of σ ($\Omega\ s^{1/2}$). EIS can be used to determine the diffusion coefficient of a Li-ion (D_{Li}) in the electrode material according to the following equation: [96]

$$D = \frac{R^2T^2}{2A^2n^4F^4C^2\sigma^2}$$

Where R is the gas constant, T is the absolute temperature, A is the active surface area of the electrode, *n* is the number of electrons per molecule during reaction, F is the Faraday constant, C is the concentration of Li^+ ion, and σ is the Warburg prefactor. Warburg

prefactor (σ) has a relationship with Warburg impedance Z_w, which is expressed as follows

$$Z_w = R_D + R_L + \sigma\omega^{-1/2}$$

Calculated from the slope of the linear fit, the apparent diffusion coefficients for the Co_3O_4/MCNT electrode is 1.8×10^{-12} cm^2 s^{-1}. This value is slightly higher than that of Co_3O_4/CNT electrode composite, where D_{Li} is 1.1×10^{-13} cm^2 s^{-1}. These results suggest that the mesoporous structure and void space of the MCNT allow for the easy penetration of the electrolyte, which results in a more thorough activation of the inside the Co_3O_4 NPs.

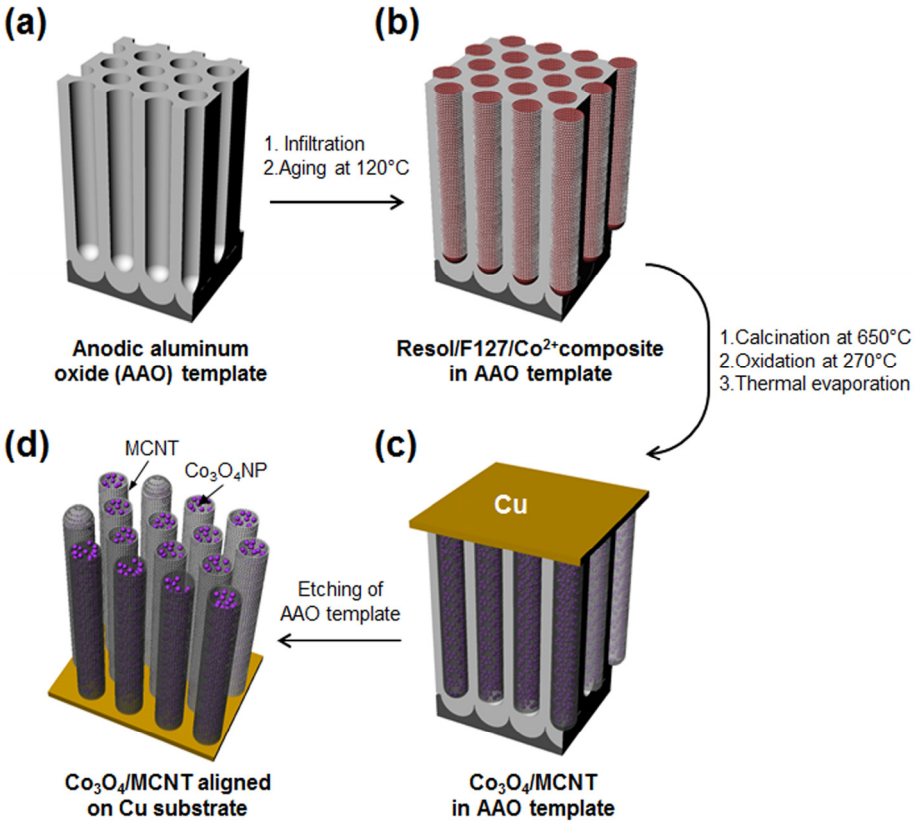

Figure 4-1 Process flow diagram for the preparation of a Co_3O_4/MCNT composite aligned on a Cu current collector using a porous AAO template.

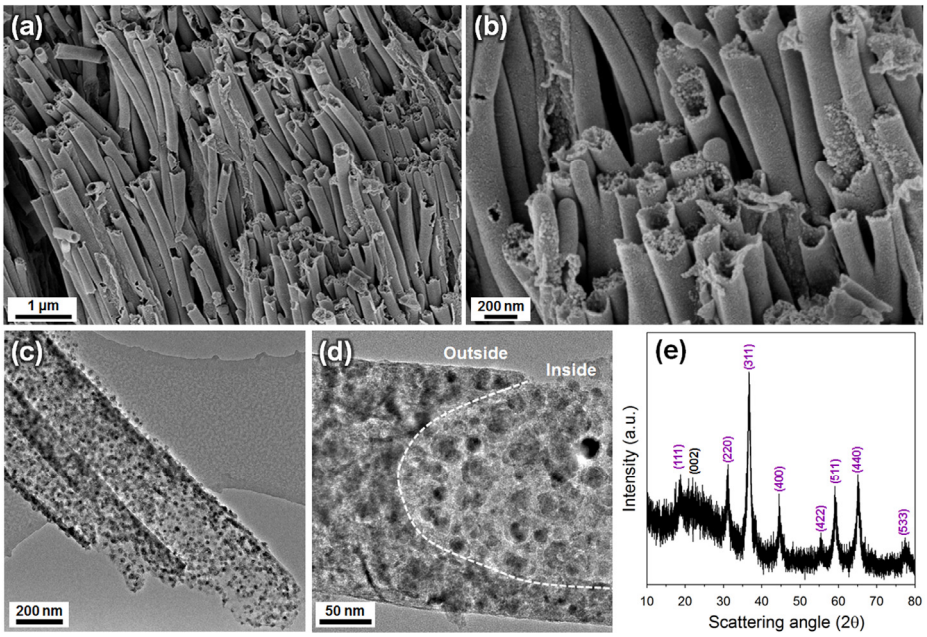

Figure 4-2 (a,b) SEM images, (c,d) TEM images, and (e) XRD pattern of the Co_3O_4/MCNTs.

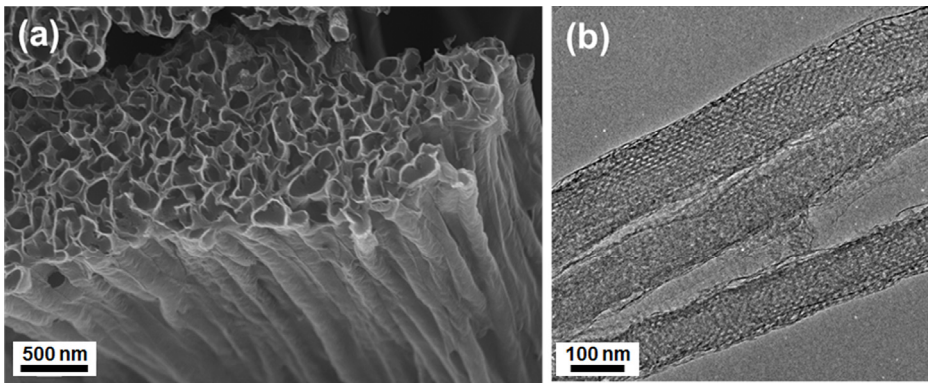

Figure 4-3 (a) SEM image and (b) HR-TEM image of MCNT

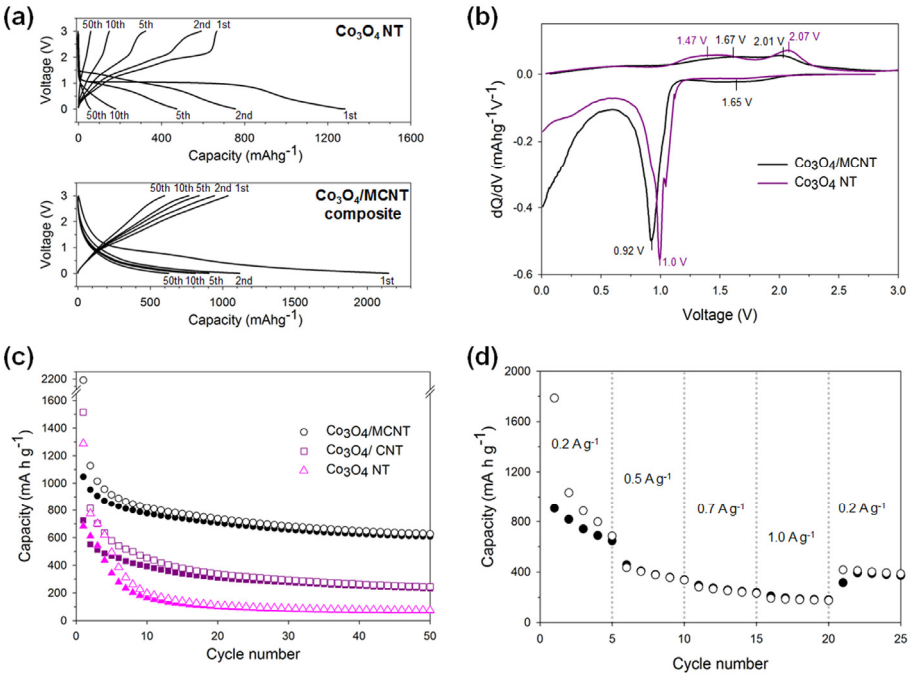

Figure 4-4 Galvanostatic charge-discharge curves of Co_3O_4 NT and Co_3O_4/MCNT cycled at the 1st, 2nd, 5th, 10th and 50th between 0.01 and 3 V(*vs* Li^+/Li) at a current density of 100 mA g^{-1}. (b) Differential capacity of Co_3O_4/MCNT and Co_3O_4 NT at the first cycle. (c) Cycling performance of the Co_3O_4/MCNT, Co_3O_4 /CNT and Co_3O_4 NT at a constant current density of 100 mA g^{-1}. (d) Rate capability for Co_3O_4/MCNT electrode.

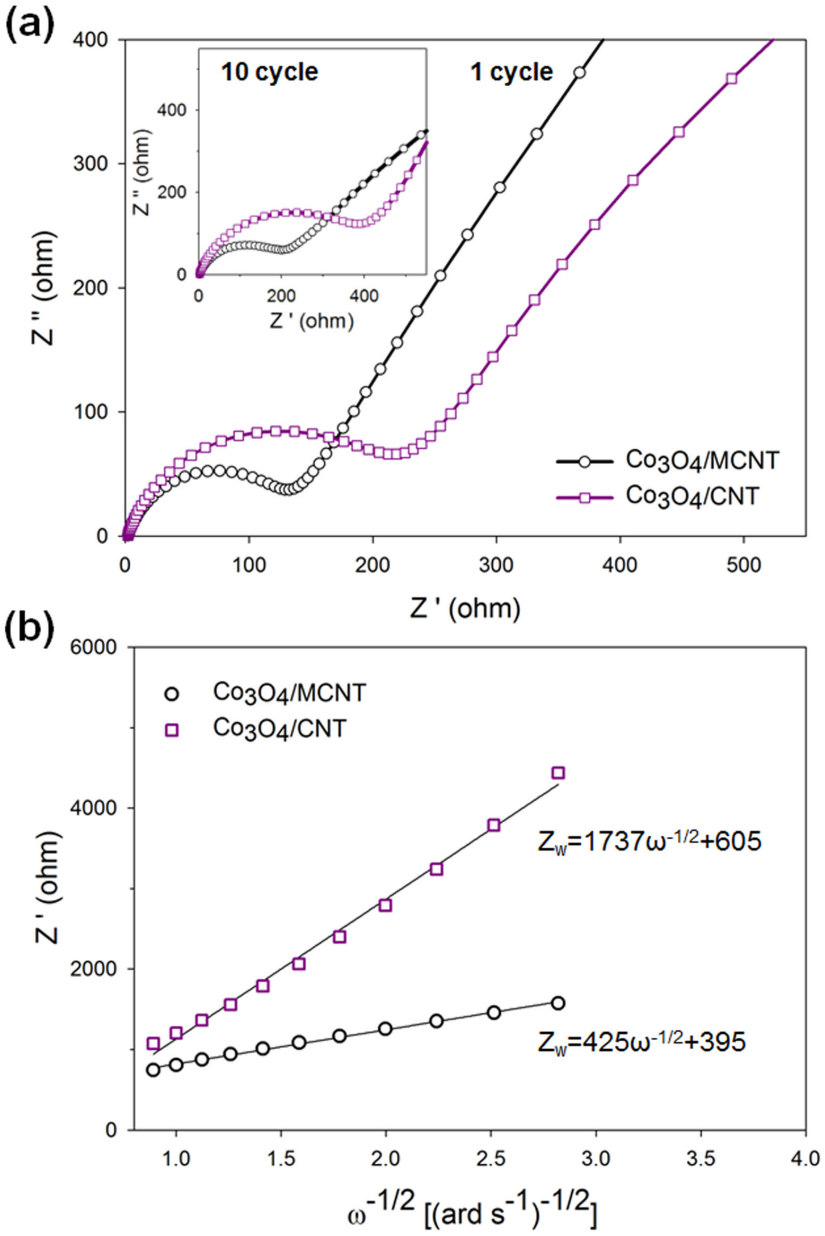

Figure 4-5 (a) Nyquist plots of the Co_3O_4/MCNT and Co_3O_4/CNT in the first cycle and after 10 cycles (inset). (b) Relationship between Z_{re} and $\omega^{-1/2}$ in the frequency region of 0.2-0.02 Hz.

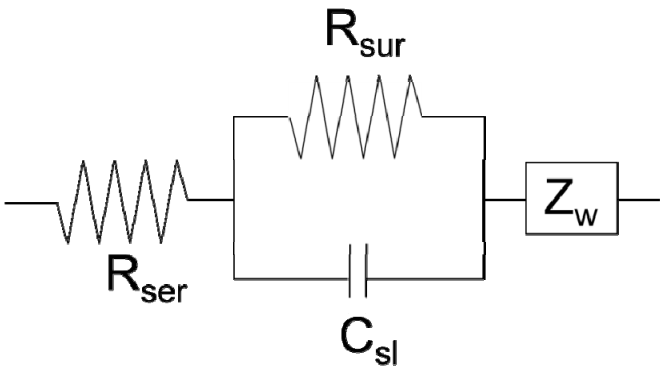

Figure 4-6 Equivalent circuit used to fit impedance fata. R_{ser} is the ohmic resistance of the electrolyte, R_{sur} is the surface and charge transfer resistance of the electrode, Q_{dl} is the double layer pseudocapacitance of the electrode, and Z_w is the Warburg impedance arising from the diffusion process inside the electrode.

Table 4-1 Impedance fitting parameters

Electrode	Cycle	R_{ser} (Ω) × 10^{-16}	R_{sur} (kΩ)	Y_0 ($\Omega^{-1}s^n$) × 10^{-5}	n
Co_3O_4/MCNT	1	2.22	0.086	2.33	0.78
	10	2.22	0.204	4.78	0.68
Co_3O_4 /CNT	1	2.22	0.156	1.35	0.83
	10	2.22	22.833	127.50	0.45

*Y_o and n are the two elements used to fit the constant phase elements Q.

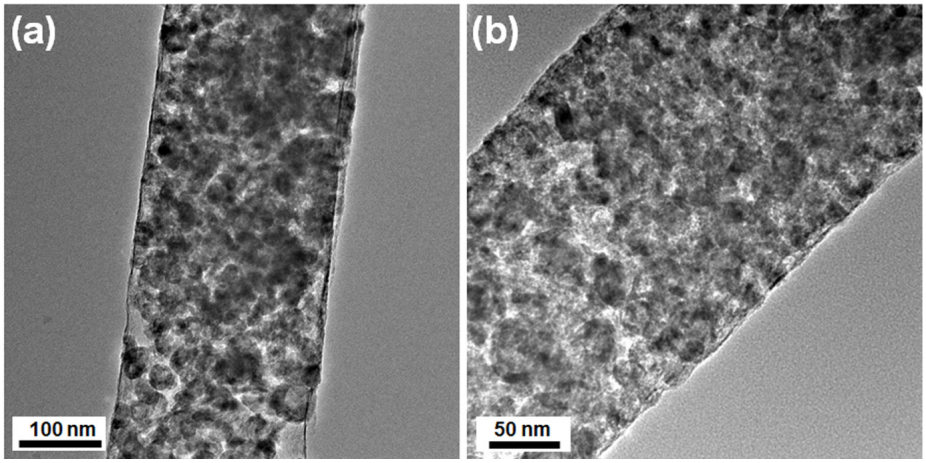

Figure 4-7 (a,b) HR-TEM images of Co_3O_4/CNT

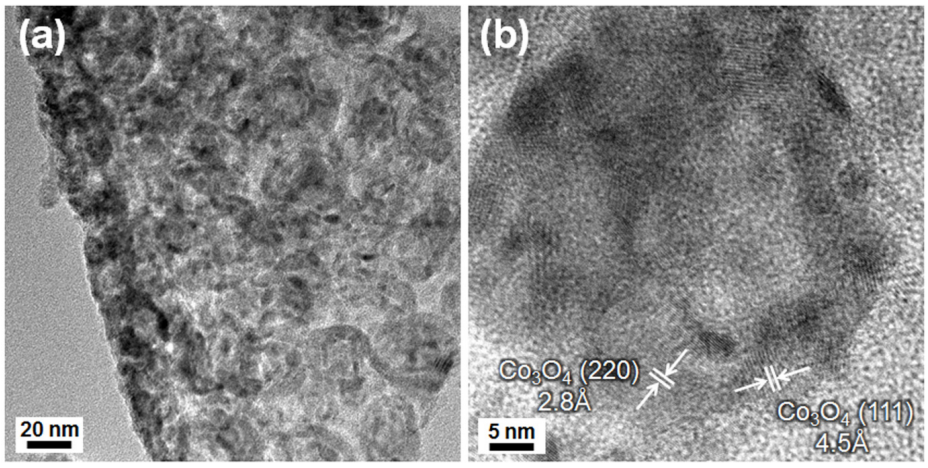

Figure 4-8 (a,b) HR-TEM images of Co_3O_4 NT

Chapter 5. Summary and Conclusions

The Si/OMC composite was prepared for use as an anode material in rechargeable Li batteries. The composite was synthesized by the self-assembly of Pluronic F127, a resorcinol-formaldehyde polymer and Si nanoparticles. The improved cycling performance of the Si/OMC composite can be attributed to the pore structure of OMC that not only absorbs the stress that arises with volume expansion of Si but also facilitate the contact of the electrolyte with Si NPs. This unique pore structure of OMC has promise as carbon matrices for replacing materials such as graphite, graphene and carbon nanotubes for metals and metal oxides to improve their electrochemical performance.

The Co_3O_4/OMC nanostructured composite has been synthesized to use as anode materials in Li-ion battery by the facile co-self-assembly strategy, which is well dispersed Co_3O_4 NPs embedded inside the wall of the OMC. The Co_3O_4/OMC composite shows a high reversible capacity of ~1025 mA h g^{-1} after 100 cycles and retains high Coulombic efficiency above ~98%, indicating improving reversible capacity and cycling stability compared to Co_3O_4@C composites and bare Co_3O_4 NPs, respectively. The results give clear evidence of advantages of the constructing composite with OMC to improve the electrochemical performance of Co_3O_4 NPs as excellent anode materials for Li-ion batteries.

The Co_3O_4/MCNT electrode was prepared for use as an anode electrode in Li-ion batteries. The composite electrode was synthesized by a dual templating method *via* the hard template of AAO membrane together with

the soft template of block copolymer surfactant F127. The Co_3O_4/MCNT electrode shows highly reversible capacity about 556 mA h g^{-1} after 100 cycles, compared with those of Co_3O_4/CNT electrode and Co_3O_4 NT electrode. These results suggest that 3-D structured carbon framework allow direct electronic pathways for efficient charge transport and well-dispersed Co_3O_4 NPs in the MCNT is useful to diminish of surface resistance through the formation stable SEI layer.

These results show that the unique 3-D nanosturcred carbon composite prepared by solvent evaporation induced co-self-assembly method has promise as anode materials for high-performance Li-ion batteries.

Chapter 6. Recommendations for Further Research

The recommendations for further research are summarized as follows;

1) Transition metal oxides have been focused on as anode materials for Li-ion batteries due to their high electrochemical capacities compared to carbonaceous materials. Among diverse metal oxides, abundant, low cost and environmentally benign material such as TiO_2 and Fe_2O_3 can be useful to hybridizing with 3-D nanostructured mesoporous carbon.
2) In the hard templating method, the preventing aggregation and collapsing of the nanotubes is important. The nanotubes tend to lose their well-aligned orientation during the wet-chemical etching due to the capillary forces between the nanotubes upon drying. The retention of the integrity of the arrays of free standing nanotubes after removal of the template will be key issues using AAO templates controlled precisely pore length and diameter
3) It is necessary to understand the kinetics of Li ion migration through surface of electrode, charge transfer on solid/electrolyte interfaces, and further diffusion in electrode material since these processes indeed govern the polarization and reaction rate of 3d transition meal oxide. Therefore, further study will be required to measure and analyze using the *in-situ* XRD, the *in situ* XPS, and an electrochemical impedance spectroscopy (EIS).

Bibliography

[1] D. Linden, and T. B. Reddy, *Handbook of Batteries,* McGraw-Hill, New York, 2002, 3rd edn., ch.35, pp. 35.1.

[2] R. A. Huggins, and *Advanced Batteries; Materials Science Aspects*, Springer, New York, 2009, ch.7, pp. 123-149.

[3] M. Roberts , P. Johns , J. Owen , D. Brandell , K. Edstrom , G. El Enany , C. Guery , D. Golodnitsky , M. Lacey , C. Lecoeur , H. Mazor , E. Peled , E. Perre , M. M. Shaijumon , P. Simon , and P. -L. Taberna, *J. Mater. Chem.,* **21**, 9890 (2011).

[4] L. Dimesso, C. Förster, W. Jaegermann, J. P. Khanderi, H. Tempel, A. Popp, J. Engstler, J. J. Schneider, A. Sarapulova, D. Mikhailova, L. A. Schmitt, S. Oswald, and H. Ehrenberg, *Chem. Soc. Rev.,* **41**, 5068 (2012).

[5] M. Choi, and R. Ryoo*, Nat. Mater.,* **2***,* 473 (2003).

[6] W. Kim, N. D. Kim, M. Y. Kang, J. B. Joo, I. K. Song, J. R. Yoon, and J. Yi, *Carbon,* **48**, 4556 (2010).

[7] M. Hartmann, *Chem. Mater*., **17**, 4577 (2005).

[8] H. S. Zhou, S. M. Zhu, M. Hibino, I. Honma, and M. Ichihara, Adv. Mater., **15**, 2107 (2003).

[9] R. Ryoo, S. H. Joo, M. Kruk, and M. Jaroniec, *Adv. Mater*., **13**, 677 (2001).

[10] C. J. Brinker, Y. Lu, A. Sellinger, and H. Fan, *Adv. Mater*., **11**, 579 (1999).

[11] H. Yang, A. Kuperman, N. Coombs, S. Mamiche-Afara, and G. A. Ozin, *Nature*, **379**, 703 (1996).

[12] C. Liang, K. Hong, G. A. Guiochon, J. W. Mays, and S. Dai, *Angew.*

Chem. Int Ed., **43**, 5785 (2004).

[13] S. Tanaka, Y. Nishiyama, K. Egashira, and K. Ueyama, *Chem. Commun.,***16**, 2125 (2005)

[14] Y. Meng, D. Gu, F. Q. Zhang, Y.F. Shi, H. F. Yang, Z. Li, C. Z. Yu, B. Tu, and D. Y. Zhao, *Angew. Chem. Int Ed.,* **117**, 7215 (2005).

[15] D. Grosso, F. Cagnol, G. Soler-Illia, E. L. Crepaldi, H. Amenitsch, A. Brunet-Bruneau, A. Bourgeois, and C. Sanchez, *Adv. Funct. Mater.,* **14**, 309 (2004).

[16] C. Rodriguez-Abreu, N. Vilanova, C. Solans, M. Ujihara, T. Imae, A. López-Quintela, and S. Motojima, *Nanoscale Res. Lett.*, **6**, 330 (2011).

[17] S. J. Hurst, E. K. Payne, L. Qin, and C. A. Mirkin, *Angew. Chem. Int Ed.*, **21**, 2672 (2006).

[18] J. -M. Tarascon, *Nat. Chem*., **2** 510 (2010).

[19] M. T. McDowell, S. W. Lee, I. Ryu, H. Wu, W. D. Nix, J. W. Choi, and Y. Cui, *Nano Lett.,* **11**, 4018 (2011).

[20] M. -H. Park, M. G. Kim, J. Joo, K. Kim, J. Kim, S. Ahn, Y. Cui, and J. Cho, *Nano Lett.,* **9**, 3844 (2009)

[21] C. K. Chan C K, Peng H, Liu G, McIlwrath K, Zhang X F, Huggins R A and Cui Y, *Nat.Nano.,* **3**,31 (2008).

[22] L. F. Cui, Y. Yang, C. M. Hsu, and Y. Cui, *Nano Lett.,* **9**, 3370 (2009).

[23] J. K. Lee, K. B. Smith, C. M. Hayner, H. H. Kung, *Chem. Commun*., **46**, 2025 (2010).

[24] W. Xu, and J. C. Flake, *J. Electrochem. Soc.,* **157**, A41 (2010).

[25] B. Hertzberg, A. Alexeev, and G. Yushin, *J. Am. Chem. Soc.,* **132**, 8548 (2010).

[26] L. Ji, and X. Zhang, *Electrochem. Commun.,* **11**, 1146 (2009).

[27] J. R. Szczech, and S. Jin, *Energy Environ. Sci.,* **4** 56 (2011).

[28] X. Ji, K. T. Lee, and L. F. Nazar, *Nat. Mater*., **8**, 500 (2009).

[29] M. –Y. Cheng, and B. –J. Hwang, *J. Power Sources,* **195**, 4977 (2010).

[30] H. Zhang, H. Tao, Y. Jiang, Z. Jiao, M. Wu and B. Zhao, *J. Power Sources,* **195**, 2950 (2010).

[31] S. Zhu, H. Zhou, M. Hibino, I. Honma, and M. Ichihara, *Adv. Funct. Mater.,* **15**, 381 (2005).

[32] R. Ryoo, S. H. Joo, and S. Jun, *J. Phys. Chem. B,* **103**, 7743 (1999).

[33] J. Wang, C. Xue,Y. Lv, F. Zhang, B. Tu and D. Zhao, *Carbon,* **49**, 4580 (2011).

[34] Y. Meng, D. Gu, F. Zhang, Y. Shi, L. Cheng, D. Feng, Z. Wu, Z. Chen, Y. Wan, A. Stein, and D. Zhao, *Chem. Mater*., **18**, 4447 (2006).

[35] W. Gao, Y. Wan, Y. Dou and D. Zhao, *Adv. Energy Mater*., **1**, 115 (2011).

[36] S. Jun, S. H. Joo, R. Ryoo, M. Kruk, M. Jaroniec, Z. Liu, T. Ohsuna, and O Terasaki, *J. Am. Chem. Soc.,* **122**, 10712 (2000).

[37] Y. Meng, D. Gu, F. Zhang, Y. Shi, H. Yang, Z. Li, C. Yu, B. Tu, and D. Zhao, *Angew. Chem. Int. Ed*., **44**, 7053 (2005).

[38] Y. –S. Hu, R. Demir-Cakan, M. –M. Titirici, J. –O. Müller, R. Schlögl, M. Antonietti, and J. Maier, *Angew. Chem. Int. Ed*., **47**, 1645 (2008).

[39] H. Yang, Y. Yan, Y. Liu, F. Zhang, R. Zhang, Y. Meng, M. Li, S. Xie, B. Tu, and D. Zhao, *J. Phys. Chem. B,* **108**, 17320 (2004).

[40] D. Zhao, J. Feng, Q. Huo, N. Melosh, G. H. Fredrickson, B. F. Chmelka, and G. D. Stucky, *Science,* **279**, 548 (1998).

[41] M. N. Obravac, and J. Krause, *J. Electrochem. Soc.,* **154**, A103 (2007).

[42] N. Liu, H. Wu, M. T. McDowell, Y. Yao, C. Wang, and Y. Cui, *Nano Lett.,* **12**, 3315 (2012).

[43] K. J. Lee, K. B. Smith, C. M. Hayner, and H. H. Kung, *Chem. Commun.,* **46**, 2025 (2010).

[44] M. K. Datta, and P. N. Kumta, *J. Power Sources,* **194**, 1043 (2009).

[45] S. –H. Ng, J. Wang, D. Wexler, K. Konstantinov, Z. –P. Guo, and H. –K. Liu, *Angew. Chem. Int. Ed.,* **45**, 6896 (2006).

[46] J. P. Maranchi, A. F. Hepp, A. G. Evans, N. T. Nuhfer, and P. N. Kumta, *J. Electrochem. Soc.,* **153***,* A1246 (2006).

[47] Y. –D. Cho, G. T. –K. Fey, and H. -M. Kao, *J. Power Sources,* **189**, 256 (2009).

[48] H. Wu, G. Zheng, N. Liu, T. J. Carney, Y. Yang, Y. Cui, *Nano Lett.,* **12**, 904 (2012).

[49] P. Poizot, S. Laruelle, S. Grugeon, L. Dupont, and J. -M. Tarascon, *Nature,* 2000, **407**, 496 (2000).

[50] J. Cabana, L. Monconduit, D. Larcher, and M. R. Palacin, *Adv. Mater.*, **22**, E170 (2010).

[51] Y. Liu, C. Mi, L. Su, and X. Zhang, *Electrochim. Acta,* **53**, 2507 (2008).

[52] P. G. Bruce, B. Scrosati, and J. –M. Tarascon, *Angew. Chem. Int. Ed.,* **47**, 2930 (2008).

[53] Y.-G. Guo, J. -S. Hu, and L. -J. Wan, *Adv. Mater.,* **20**, 2878 (2008).

[54] H. -J. Liu, S. -H. Bo, W. -J. Cui, F. Li, C.-X. Wang, and Y. -Y. Xia, *Electrochim. Acta*, **53**, 6497 (2008).

[55] H. Qiao, L. Xiao, Z. Zheng, H. Liu, F. Jia, and L. Zhang, *J. Power Sources*, **185**, 486 (2008).

[56] G.Wang, X. Shen, J. Yao, D. Wexler, and J. Ahn, *Electrochem. Commun.*, **11**, 546 (2009).

[57] S. Yang, X. Feng, S. Ivanovici, and K. Müllen, *Angew. Chem. Int. Ed.,* **49**, 8408 (2010).

[58] Z. -S. Wu, W. Ren, L. Wen, L. Gao, J. Zhao, Z. Chen, G. Zhou, F. Li, and H. -M. Cheng, *ACS Nano*, **4**, 3187 (2010).

[59] G. -P. Kim, I. Nam, N. D. Kim, J. Park, S. Park, and J. Yi, *Electrochem. Commun.*, **22**, 93 (2012).

[60] T. Yu, Y. Deng, L. Wang, R. Liu, L. Zhang, B. Tu, and D. Zhao, *Adv. Mater.,* **19**, 2301(2007).

[61] J. Wang, C. Xue, Y. Lv, F. Zhang, B. Tu and D. Zhao, *Carbon*, **49**, 4580 (2011).

[62] Y. Wang, H. J. Zhang, L. Lu, L. P. Stubbs, C. C. Wong , and J. Lin, *ACS Nano*, **4**, 4753 (2010).

[63] Ö. Çelik, and Ö. Dag, *Angew. Chem. Int. Ed.*, **113**, 3916 (2001).

[64] J. R. A. Sietsma, J. D. Meeldijk, J. P. den Breejen, M. Versluijs-Helder, A. J. van Dillen, P. E. de Jongh, and K. P. de Jong, *Angew. Chem. Int. Ed.*, **46**, 4547 (2007).

[65] W. Wang, H. Wang, W. Wei, Z. -G. Xiao, and Y. Wan, *Chem. Eur. J.,* **17**, 13461 (2011).

[66] K. S. W. Sing, D. H. Everett, R. A. W. Haul, L. Moscou, R. A. Pierotti, J. Rouquerol, and T. Siemieniewska, *Pure Appl. Chem.,* **57**, 603 (1985).

[67] E. McCafferty, and J. P. Wightman, *Surf. Interface Anal.,* **26**, 549 (1998).

[68] G. Bhargava, I. Gouzman, C. M. Chun, T.A. Ramanarayanan, and S. L. Bernasek, *Appl. Surf. Sci.,* **253**, 4322 (2007).

[69] B. P. Payne, M. C. Biesinger, and N. S. McIntyre, *J. Electron Spectrosc. Relat. Phenom.*, **184**, 29 (2011).

[70] S. C. Petitto, E. M. Marsh, G. A. Carson, and M. A. Langell, *J. Mol. Catal A- Chem.,* **281**, 49 (2008).

[71] Y. -M. Kang, K. -T. Kim, K. -Y. Lee, S. -J. Lee, J. -H. Jung, and J. -Y. Lee, *J. Electrochem. Soc.,* **150**, A1538 (2003).

[72] S. Laruelle, S. Grugeon, P. Poizot, M. Dolle, L. Dupont, and J. -M. Tarascon, *J. Electrochem. Soc.,***149**, A627 (2002).

[73] Z. Yuan, F. Huang, C. Feng, J. Sun, and Y. Zhou, *Mater. Chem. Phys.,* **79**, 1 (2003).

[74] H. -J. Liu, S. -H. Bo, W. -J. Cui, F. Li, C. -X.Wang, and Y. -Y. Xia, *Electrochim. Acta,* **53**, 6497 (2008).

[75] W. L. Yao, J. Yang, J. L. Wang , and Y. Nuli, *J. Electrochem. Soc.,* **155**, A903 (2008).

[76] M. M. Thackeray, S. D. Baker, and K. T. Adendorff, *Solid state Ionics,* **17**, 175 (1985).

[77] D. Larcher, G. Sudant, J. B. Leriche, Y. Chabre, and J.- M. Tarascon, *J. Electrochem. Soc.,* **149**, A234 (2002).

[78] H. -C. Liu, and S. -K. Yen, *J. power sources*,**166**, 478 (2007).

[79] S. grugeon, S. Laruelle, S. Grugeon, L. Dupont, P. Poizot, and J. -M. Tarascon, *J. Electrochem. Soc*., **148**, A285 (2001).

[80] M. Dollé, P. Poizot, L. Dupont, and J. M. Tarascon, *Electrochem. Solid-State Lett.,* **5**, A18 (2002).

[81] Y. Yu, C. H. Chen, J. L. Shui, and S. Xie, *Angew. Chem., Int. Ed.,* **44**, 7085 (2005).

[82] K. M. Shaju, F. Jiao, A. De´bart, and P. G. Bruce, *Phys. Chem. Chem. Phys.,* **9**, 1837 (2007).

[83] A. J. Bard, L. R. Faulkner, *Electrochemical Methods: Fundamentals and Applications,* Wiley, New york, 2nd edn., 2001, ch.6, pp.231.

[84] A. S. Aricò, P. Bruce, B. Scrosati, J.-M. Tarascon and W. V. Schalkwijk, *Nature Mater.,* **4**, 366 (2005).

[85] P. L. Taberna, S. Mitra, P. Poizot, P. Simon and J. -M. Tarason, *Nature Mater.*, **5**, 567 (2006).

[86] K. Wang, Y. Wang, Y. Wang, E. Hosona, and H. Zhou, *J. Phys. Chem. C*, **113**, 1093 (2009).

[87] G. Zhao, J. He, C. Zhang, J. Zhou, X. Chen, and T. Wang, *J. Phys. Chem. C*, **112**, 1028 (2008).

[88] J. Cho, *J. Mater. Chem*., **20**, 4009 (2010).

[89] C. S. Wang, G. T. Wu, and W. Z. Li., *J. Power. Sources*, **76**, 1 (1998).

[90] R. Ruffo, S. S. Hong, C. K. Chan, R. A, Huggins, and Y. Cui, *J. Phys. Chem. C*, **113**, 11390 (2009).

[91] D. Aurbach, B. Markovsky, M. D. Levi, E. Levi, A. Schechter, M. Moshkovich, and Y. Cohen, *J. Power Sources*, **95**, 81 (1999).

[92] J. Y. Song, H. H. Lee, Y. Y. Wang, and C. C. Wan, *J. Power Sources*, **111**, 255 (2002).

[93] D. Aurbach, M. D. Levi, E. Levi, and A. Schechter, *J. Phys. Chem. B*, **101**, 2195 (1997).

[94] S. A. Needham, G. X. Wang, K. Konstantinov, Y. Tournayre, Z. Lao, and H. K. Liu, *Electrochem. Solid-State Lett*., **9**, A315 (2006).

[95] J. Fan, and P.S. Fedkiw, *J. Power Sources*, **72**,165 (1998).

[96] J. Y. Xiang , J. P. Tu, Y. Q. Qiao, X. L. Wang , J. Zhong , D. Zhang ,

and C.D. Gu, *J. Phys. Chem. C*, **115**, 2505 (2011).

요약(국문초록)

전기자동차, 차세대 전자기기 및 재생 에너지원과 같은 분야에서 고성능 리튬이차전지는 반드시 필요한 기술이다. 이 학위논문에서는 리튬이차전지의 음극 소재와 전극으로 사용하기 위하여 3차원 나노구조의 규칙성 중형기공성 탄소 복합체의 제조법을 제안하였다. 이 제법을 통해 양친성 블락 공중고분자(연질주형)과 레조시놀-포름알데하이드 수지(탄소전구체)와 함께 금속 전구체를 사용하여 간단하게 단일 반응기에서 제조가 가능하였다. 이와 관련된 세부 결과에 대한 요약은 아래와 같다.

첫 번째, 용매 증발에 의한 유도 자기조립을 통해 규칙성 중형기공성 탄소 내에 갇혀있는 Si 나노입자 복합체를 단일 반응기에서 제조하였다. 수소결합에 의해 양친성 블락 공중고분자/페놀수지에 갇혀있던 Si 나노입자는 탄화과정을 거쳐 규칙성 중형기공성 탄소 내에 분산되었다. 제조된 복합체는 향상된 전기화학적 특성을 보였으며 균일한 기공 채널 속에 형성된 공간을 통해 Si 부피팽창의 충격완화 효과와 실린더 형태의 균일한 기공구조을 통해 리튬 이온의 급속한 확산이 이루어짐을 보였다.

두 번째, 약 10 nm 이하의 평균크기를 갖는 Co_3O_4 나노입자가 균일하

게 분포된 규칙성 중형기공성 탄소 복합체를 제조하였다. 리튬이차전지의 음극소재로서의 높은 성능을 보였으며 이는 고르게 분산된 Co_3O_4나노입자의 증가된 전하저장능력과 관계가 있음을 보였다.

세 번째, 양친매성 계면활성제(F127)를 연질주형으로 사용하고, 양극산화알루미늄(AAO)을 경질주형으로 사용한 이중주형법으로 Co_3O_4나노입자로 채워진 중형기공성 탄소나노튜브 전극을 제조하였다. 제조된 전극은 3차원 구조의 탄소틀이 효과적인 전하이동을 위한 경로를 제공하고 중형기공성 탄소나노튜브 속에 고르게 분산된 Co_3O_4나노입자가 안정적인 SEI층 형성에 따른 표면저항 감소를 유도하기 때문에 높은 가역용량을 보임을 실험을 통해 검증하였다.

주요어: 음극용 소재, 탄소 나노섬유, 리튬이온 전지, 규칙성 중형기공성 탄소, 페놀 수지, 3차원 나노구조

학 번: 2009-30243